

## DIRECT BLIND DECONVOLUTION\*

ALFRED S. CARASSO†

**Abstract.** Blind deconvolution seeks to deblur an image without knowing the cause of the blur. Iterative methods are commonly applied to that problem, but the iterative process is slow, uncertain, and often ill-behaved. This paper considers a significant but limited class of blurs that can be expressed as convolutions of two-dimensional symmetric Lévy “stable” probability density functions. This class includes and generalizes Gaussian and Lorentzian distributions. For such blurs, methods are developed that can detect the point spread function from one-dimensional Fourier analysis of the blurred image. A separate image deblurring technique uses this detected point spread function to deblur the image. Each of these two steps uses direct noniterative methods and requires interactive tuning of parameters. As a result, blind deblurring of  $512 \times 512$  images can be accomplished in minutes of CPU time on current desktop workstations. Numerous blind experiments on synthetic data show that for a given blurred image, several distinct point spread functions may be detected that lead to useful reconstructions.

**Key words.** image deblurring, blind deconvolution, direct methods, Lévy density functions, SECB method, BEAK method, APEX method

**AMS subject classifications.** 35R25, 35B60, 60E07, 68U10

**PII.** S0036139999362592

**1. Introduction.** Blind deconvolution seeks to deblur an image without knowing the cause of the blur. This paper considers a significant but limited class of blurs and develops methods for detecting the system point spread function by appropriate Fourier analysis of the blurred image. This detected point spread function is then input into an image deblurring procedure to produce the deblurred image. Each of these two separate tasks uses direct noniterative algorithms. As a result, blind deblurring of  $512 \times 512$  images can be accomplished in minutes of CPU time on current desktop workstations. The methods are applicable in the presence of noise. Reconstructions obtained in this fashion are usually good enough for immediate use. However, if necessary these can be further refined by using them as initial values in iterative blind restoration algorithms.

Blind deconvolution is a difficult problem that is not fully understood. Nonuniqueness is compounded with discontinuous dependence on data due to ill-posedness in the deblurring problem. So far, most approaches to blind deconvolution have been iterative in nature. Because of the underlying analytical difficulties, no convergence proofs are known. In fact, the iterative process is generally ill-behaved and may develop stagnation points or diverge altogether. When the iterative process is stable, a large number of iterations may be necessary to resolve fine detail. As in all inverse problems, successful blind restoration depends on input parameters that properly restrict the class of admissible solutions. Several trial solutions based on different parameter choices are typically necessary before obtaining the correct answer. When

---

\*Received by the editors October 25, 1999; accepted for publication (in revised form) July 13, 2000; published electronically April 18, 2001. This work was performed by an employee of the U.S. Government or under U.S. Government contract. The U.S. Government retains a nonexclusive, royalty-free license to publish or reproduce the published form of this contribution, or allow others to do so, for U.S. Government purposes. Copyright is owned by SIAM to the extent not limited by these rights.

<http://www.siam.org/journals/siap/61-6/36259.html>

†Mathematical and Computational Sciences Division, National Institute of Standards and Technology, Gaithersburg, MD 20899 (alfred.carasso@nist.gov).

each trial solution requires a long and uncertain iterative process, location of optimal parameters presents serious difficulties. For this reason, blind deconvolution examples in the literature usually involve simple images of small size. Complex high resolution images of size  $512 \times 512$  or larger do not appear feasible with current approaches. One application for the methods presented here would be speeding up such iterative procedures by providing a good initial guess.

The present paper does not attempt to solve the blind deconvolution problem in full generality. Rather, attention is focused on a class of blurs, the class **G** defined below. This is a wide class that includes and generalizes Gaussian and Lorentzian distributions, and has important applications. However, out of focus and motion blurs are not included in **G**. Likewise, a large class of sharp images is exhibited and characterized in terms of its behavior in the Fourier domain. This is the class **W** described below. It is shown how one-dimensional (1-D) Fourier analysis of blurred image data can be used to detect class **G** point spread functions acting on class **W** images. Lévy “stable” probability density functions play a central role in this analysis. The paper is based on empirical observations about the class **W** that have not previously been exploited in the literature.

The Fourier approach presented here is helpful in clarifying the role of noise as it separately affects the detection and reconstruction problems. It also leads naturally to the *BEAK method* of detection for class **W** images, based on a new type of a priori information. This information involves the “gross behavior” of the sharp image along a single line through the origin in the Fourier transform plane. For class **W** images, such gross behavior can be summarized by two positive numbers. As noted in section 7 and discussed more fully in [8], there are several practical contexts where such information may be available, or may be reliably estimated.

The more generally applicable *APEX method* is discussed in section 8. This method may be applied without prior knowledge of gross behavior in the sharp image, provided that image is a recognizable object. The procedure requires interactive adjustment of a key parameter. However, each such trial solution can be accomplished in seconds of CPU time. Important additional flexibility is provided by the *marching backward in time* option characteristic of class **G** point spread functions.

These two procedures are illustrated with several numerical experiments on synthetically blurred images, with added noise. Numerous other experiments with the APEX method, on a wide variety of images and point spread functions, show that for a given blurred image several distinct point spread functions may be detected that lead to useful reconstructions.

**1.1. Image deblurring.** In the simplest case, image deblurring is associated with the solution of two-dimensional (2-D) convolution equations

$$(1.1) \quad Hf \equiv \int_{R^2} h(x-u, y-v)f(u, v)dudv \equiv h(x, y) \otimes f(x, y) = g(x, y),$$

where  $g(x, y)$  is the recorded blurred image,  $f(x, y)$  is the desired unblurred image,  $h(x, y)$  is the blurring kernel or point spread function (psf) of the imaging process, and  $\otimes$  denotes convolution. The psf  $h(x, y)$  represents the cumulative effects of all distortions caused by the media through which signals propagate, as well as all optical and electronic aberrations produced by imperfect sensing and recording equipment. In many applications,  $h(x, y)$  is known or may be obtained experimentally by imaging a known point source. It is assumed that  $h(x, y)$  is such that the linear problem

$Hf = g$  has at most one solution. This is the case for the class of point spread functions described in section 3.

The blurred image  $g(x, y)$  includes noise, which is viewed as a separate additional degradation,

$$(1.2) \quad g(x, y) = g_e(x, y) + n(x, y),$$

where  $g_e(x, y)$  is the blurred image that would have been recorded in the absence of noise, and  $n(x, y)$  represents the cumulative effects of all noise processes and other errors affecting final acquisition of the digitized array  $g(x, y)$ . This includes nonlinear noise processes where  $n(x, y)$  may be a function of  $f(x, y)$ . Both  $g_e(x, y)$  and  $n(x, y)$  are unknown, but  $n(x, y)$  may be presumed small. The unique solution of (1.1) when the right-hand side is  $g_e(x, y)$  is the exact sharp image denoted by  $f_e(x, y)$ . Thus,

$$(1.3) \quad h(x, y) \otimes f_e(x, y) = g_e(x, y).$$

The integral equation problem (1.1) is generally ill-posed, and the presence of noise in the data presents serious difficulties. The strategy is to avoid the unique solution of (1.1). Instead we look for some approximate solution  $f^\dagger$  such that the  $L^2$ -norm  $\|f^\dagger - f_e\|$  is small. A discussion of the merits of several linear and nonlinear algorithms for approximately solving (1.1) when  $h(x, y)$  is known may be found in [6]. The direct SECB method used in this paper is outlined in section 4, with references to [3], [4], and [5].

The case where the blurring kernel is not shift invariant is considerably more difficult and is not considered in this paper.

**2. Blind deconvolution.** In several instances, the imaging process leading to  $g(x, y)$  is not fully understood, and the psf  $h(x, y)$  is unknown in (1.1). Given the noisy blurred image  $g(x, y)$ , blind deconvolution seeks to simultaneously reconstruct both  $h(x, y)$  and the unknown image  $f(x, y)$  in (1.1). Here, a priori constraints are placed on  $h$  and  $f$  to reduce the multiplicity of solutions. Even so, the problem remains fraught with difficulties. It is pointed out in [22] that the Fourier phase problem of recovering an image from the modulus of its Fourier transform is a special case of (1.1), namely

$$(2.1) \quad f(x, y) \otimes \overline{f(-x, -y)} = g(x, y).$$

The latter problem is more easily solved in two dimensions than it is in one dimension, where severe nonuniqueness prevails [10], [15], hence the claim in [22] that blind deconvolution is not theoretically feasible in fewer than two dimensions. Numerical experience with 1-D problems tends to support that claim. In [21], uniqueness in 2-D blind deconvolution is analyzed by considering the Fourier magnitude problem.

Most blind approaches to (1.1) are iterative in nature, and typically involve nonnegativity and/or support constraints on the components  $h$  and  $f$ . In [1], beginning with a nonnegative guess for one of the components, say  $f$ , (1.1) is solved for  $h$  using FFT algorithms. Nonnegativity and  $L^1$ -norm conservation are then enforced on  $h$ . The resulting  $h$  is now fed back into (1.1) which is solved to produce a new estimate for  $f$ , and so on. According to [22], this method can diverge, with the new estimates becoming visually worse than the preceding ones. In [11], the basic deconvolution step in [1] is accomplished using Wiener filtering. A support constraint is also incorporated. This permits blind deconvolution of noisy complex-valued images, provided these images are relatively simple. When the support constraint in [11] is

replaced by a nonnegativity constraint, the algorithm is found to behave poorly in the presence of noise, sometimes producing unrecognizable reconstructions [14]. Better noise tolerance is found if deconvolution at each iterative step in [1] is accomplished using the Lucy–Richardson method [14]. The latter is itself an iterative procedure that automatically preserves nonnegativity and conserves the  $L^1$ -norm. Approximately 10 Lucy–Richardson iterations within one blind iteration were found necessary in [14]. Such an approach is viable in the context discussed in [14] where small size images of simple objects are considered, and the primary aim is object recognition. For larger images of complex objects, the Lucy–Richardson method often requires thousands of iterations to resolve fine detail [6] and may not be suited for blind deconvolution.

Several blind procedures are based on minimizing an appropriate cost functional, and this minimum must be found iteratively. Various linear and nonlinear functionals are explored in [9], [20], [22], [24], [26], and [27], and examples of successful blind deconvolution are given. However, following work in [25] on the Fourier phase problem, several authors caution against the possibility of erroneous solutions associated with local minima of the cost functional. In [22], conjugate gradient minimization of a particular cost functional is proposed, and the method is demonstrated for simple images. For more complicated objects, the author points out that there may be a multiplicity of solutions, each corresponding to a local minimum of the error functional. The same difficulty is stressed in [24], where a different cost functional is used. To circumvent stagnation at local minima, the Monte Carlo global minimization technique known as *simulated annealing* is advocated in [24] and applied to small images. Such an approach quickly becomes impractical for larger images. In the functional proposed in [26], the authors again note the possibility of stagnation at local minima. The phenomenon of successive psf iterates  $h^n$  converging to the Dirac  $\delta$ -function, with the corresponding restorations  $f^n$  converging to the original blurred image  $g$ , is reported in [22] and [14], where substantially different algorithms are discussed.

Clearly, at the present time, blind deconvolution is too new and too difficult a subject for there to exist highly reliable algorithms. Part of the difficulty may stem from algorithmic formulations designed to accommodate very general deconvolution problems. By restricting the class of blurs, we simplify the blind problem and other approaches become feasible. One such avenue is explored in this paper.

**3. Class G point spread functions.** Point spread functions may be viewed as 2-D probability density functions, since they are nonnegative and have unit  $L^1(R^2)$  norm. A symmetric Lévy “stable” density  $h(x, y)$  has Fourier transform given by [13], [23]

$$(3.1) \quad \hat{h}(\xi, \eta) \equiv \int_{\mathbf{R}^2} h(x, y) e^{-2\pi i(x\xi + y\eta)} dx dy = e^{-\alpha(\xi^2 + \eta^2)^\beta}, \quad \alpha > 0, \quad 0 < \beta \leq 1.$$

Such Lévy densities play a role in many important image deblurring applications. The Gaussian case, corresponding to  $\beta = 1$ , occurs in very diverse contexts including optical seekers in cruise missiles, undersea imaging, nuclear medicine, computed tomography scanners, and ultrasonic imaging in nondestructive testing. The case  $\beta = 5/6$  describes long-exposure atmospheric turbulence blurring [18] and is important in some astronomical and surveillance satellite applications. The case  $\beta = 1/2$  corresponds to the Cauchy or Lorentzian distribution. This has been used to model X-ray scattering in radiology. In addition, in astronomical “adaptive optics” systems that use deformable mirrors to compensate for turbulence, Lorentzian distributions have recently been found to best-fit empirically obtained point spread functions [12].

Values of  $\beta$  satisfying  $0 < \beta \leq 1$  characterize a wide variety of electron-optical devices [19]. Such devices are important in night vision systems, low light level TV, under-sea imaging, and many new biomedical imaging applications. References for many of these applications of Lévy densities may be found in the bibliographies of [3] and [5].

In some applications, several electron-optical devices may be cascaded together and used to image objects through a distorting medium such as the atmosphere or the ocean, or may be combined with other devices to produce a biomedical imaging tool. The overall psf is then the convolution product of the individual component psfs,

$$(3.2) \quad \hat{h}(\xi, \eta) = e^{-\sum_{i=1}^J \alpha_i (\xi^2 + \eta^2)^{\beta_i}}, \quad \alpha_i \geq 0, \quad 0 < \beta_i \leq 1.$$

The general functional form given in (3.2) may also be used to best-fit a large class of empirically determined optical transfer functions, by suitable choices of the parameters  $\alpha_i$ ,  $\beta_i$ , and  $J$ . However, other types of blurs important in applications, including out of focus and motion blurs, are not expressible in the form (3.2).

We define the class **G** of blurring kernels to be the class of all psfs  $h(x, y)$  whose Fourier transforms satisfy (3.2). With such psfs, we may define fractional powers  $H^t$ ,  $0 \leq t \leq 1$ , of the convolution integral operator  $H$  in (1.1) as follows:

$$(3.3) \quad H^t f \equiv \mathcal{F}^{-1} \left\{ \hat{h}^t(\xi, \eta) \hat{f}(\xi, \eta) \right\}, \quad 0 \leq t \leq 1.$$

Class **G** psfs are intimately related to diffusion processes, in that  $u(x, y, t) = H^t f$  is the solution at time  $t$  of a generalized diffusion equation (see (4.2) below). The present paper is exclusively concerned with such kernels. More general blurs will be considered in a later report. It should be noted that the class **G** represents only a small subclass of the class of *infinitely divisible* densities [13], [23]. The latter class includes various types of multimodal point spread functions whose correct blind identification would be difficult.

### 3.1. Approximate equivalence and nonuniqueness in blind restoration.

Approximations to class **G** point spread functions at equispaced points on a 2-D mesh can be generated using inverse FFT algorithms. Below, several such psfs are obtained in this fashion and used to construct synthetic data for blind deconvolution experiments. To construct an approximation to a pure Lévy density with given  $(\alpha, \beta)$  on a  $512 \times 512$  grid, we inverse FFT the expression  $e^{-\alpha(\xi^2 + \eta^2)^\beta}$ , with  $(\xi, \eta)$  in (3.1) viewed as discrete integer frequencies satisfying  $-256 \leq \xi, \eta \leq 256$ . Figure 1(A) is one example of such an approximate Lévy density function. A similar process applied in (3.2) generates approximations to more general class **G** psfs.

The behavior of  $\hat{h}(\xi, \eta)$  at infinity is uniquely determined by the values of  $\alpha$  and  $\beta$  in the Fourier transform expression (3.1). Accordingly, distinct pairs  $(\alpha, \beta)$  determine distinct symmetric stable densities  $h_{\alpha\beta}(x, y)$ . However, on a finite mesh, approximate Lévy densities generated by the inverse FFT procedure described above need not have this property. In limited precision arithmetic, a pair  $(\alpha_1, \beta_1)$  may produce a density that closely approximates, at mesh points, a density associated with a different pair  $(\alpha_2, \beta_2)$ . In that case, we say that the densities  $h_{\alpha_1\beta_1}(x, y)$ ,  $h_{\alpha_2\beta_2}(x, y)$  are *approximately equivalent*. An example of this phenomenon is shown in Figure 1(B), where we have superposed 1-D cross sections of densities associated with the pairs  $(0.072, 0.582)$  and  $(0.04, 0.682)$ . Note that approximate equivalence of the pairs  $(\alpha_1, \beta_1)$ ,  $(\alpha_2, \beta_2)$  requires  $\alpha_1 > \alpha_2$  and  $\beta_1 < \beta_2$ . Also, a compound class **G** psf in (3.2) may be approximately equivalent to a pure Lévy density in (3.1).

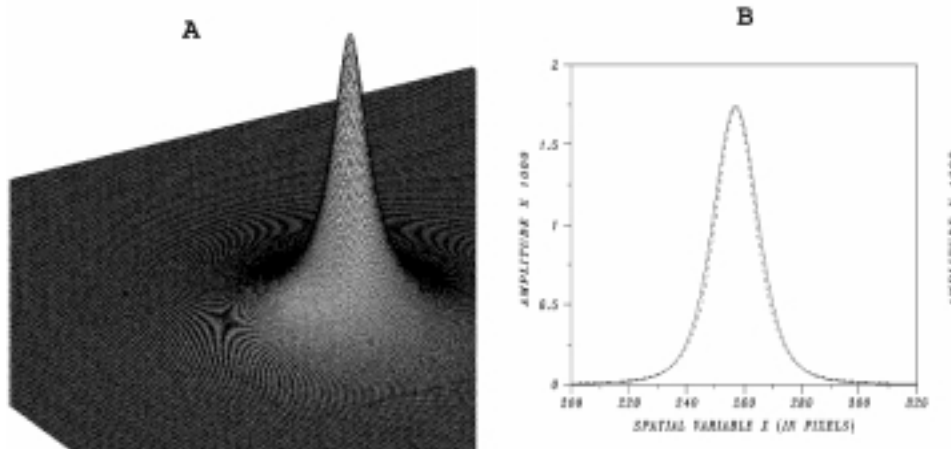


FIG. 1. (A) Lévy density function constructed by inverse FFT of  $e^{-0.75(\xi^2+\eta^2)^{1/3}}$  on  $512 \times 512$  grid, with integer  $(\xi, \eta)$ ,  $-256 \leq \xi, \eta \leq 256$ . (B) Approximate equivalence of Lévy density functions shown by superposing 1-D cross sections. Dashed curve has  $\alpha = 0.072$ ,  $\beta = 0.582$ ; solid curve has  $\alpha = 0.04$ ,  $\beta = 0.682$ .

These considerations imply an a priori nonuniqueness in blind deconvolution of digital images stored in finite precision. One cannot expect to identify the true system psf, but only a psf that is approximately equivalent to the true psf. Indeed, numerous blind deblurring experiments using the BEAK method discussed in section 7 show that while the true system psf is seldom detected, approximately equivalent psfs are commonly found.

More genuine nonuniqueness occurs if the blind deconvolution problem is understood to mean the following. Given the blurred image  $g(x, y)$  find a psf  $h(x, y)$  that leads to a useful restoration. As will be seen with the APEX method in section 8, several nonequivalent psfs may be found that lead to useful yet visually distinct reconstructions.

**4. Deblurring in class G and backward diffusion equations.** When the psf is a Gaussian, the blurred image  $g(x, y)$  may be viewed as the solution at time  $t = 1$ , of the heat equation with an appropriate *constant* diffusion coefficient,  $\lambda > 0$ . The desired deblurred image  $f(x, y)$  is the *initial data* in this heat flow problem:

$$(4.1) \quad \begin{aligned} u_t &= \lambda \Delta u, & 0 < t \leq 1, \\ u(1) &= g(x, y). \end{aligned}$$

Indeed,  $u(x, y, t) = H^t f$ ,  $0 \leq t \leq 1$ , with  $H$  being Gaussian convolution. Accordingly, deblurring Gaussian blurred images is mathematically equivalent to solving the heat equation backward in time. More generally, for psfs in class **G** as in (3.2), the heat equation in (4.1) becomes a generalized linear diffusion equation with fractional powers of the Laplacian,

$$(4.2) \quad \begin{aligned} u_t &= - \sum_{i=1}^J \lambda_i (-\Delta)^{\beta_i} u, & \lambda_i = \alpha_i (4\pi^2)^{-\beta_i}, & 0 < t \leq 1. \\ u(1) &= g(x, y). \end{aligned}$$

Such fractional diffusion equations occur in several branches of applied mathematics. See [2], [17], and references therein. In [3], [4], and [5], a method is developed and analyzed for solving diffusion equations such as (4.2) backward in time, and applied to image deblurring. This is the so-called SECB method, based on a new *slow evolution* constraint. With  $f$ ,  $g$ , and  $n$  as in (1.1), (1.2), and  $u(t)$  the solution of (4.2), let constants  $\epsilon$ ,  $M$ , be given such that

$$(4.3) \quad \|u(0) - f\| \leq M, \quad \|u(1) - g\| \leq \epsilon, \quad \epsilon \ll M.$$

For any constant  $K > 0$  such that  $K \ll M/\epsilon$  define  $s^*$  by

$$(4.4) \quad s^* = \log \{M/(M - K\epsilon)\} / \log(M/\epsilon).$$

The SECB constraint applied to the backward in time solution of (4.2) requires that there exist a known small constant  $K > 0$  and a known fixed  $s \gg s^*$ , such that

$$(4.5) \quad \|u(s) - u(0)\| \leq K\epsilon.$$

The SECB solution of the backward problem for (4.2), with noisy data  $g(x, y)$  given at time  $t = 1$ , is that initial value  $u^\dagger(0)$  that *minimizes*

$$(4.6) \quad \|u(1) - g\|^2 + (\epsilon/M)^2 \|u(0)\|^2 + K^{-2} \|u(s) - u(0)\|^2,$$

over all choices of initial values  $u(0)$  in  $L^2$ .

For a given class  $\mathbf{G}$  point spread function  $h(x, y)$  in (1.1), we may find the optimal deblurred image  $f^\dagger(x, y)$  in closed form in the Fourier transform domain. We have, with  $\bar{z}$  denoting the complex conjugate of  $z$ ,

$$(4.7) \quad \hat{f}^\dagger(\xi, \eta) = \frac{\bar{\hat{h}}(\xi, \eta) \hat{g}(\xi, \eta)}{|\hat{h}(\xi, \eta)|^2 + (\epsilon/M)^2 + K^{-2} |1 - \hat{h}^s(\xi, \eta)|^2},$$

leading to  $f^\dagger(x, y)$  upon inverse transforming. This leads to an efficient, direct numerical deblurring procedure, based on FFT algorithms. Note that it is not necessary to know  $\hat{h}(\xi, \eta)$  explicitly as in (3.2) in order to use this method, although theoretical development of the method is based on the functional form (3.2). Indeed, given the blurred image and point spread function arrays in *real space*, FFT algorithms can be used to form the expression in (4.7). On the other hand, in the case of *blind deconvolution*, the detection procedures discussed below operate in the Fourier domain, and provide approximate values for the psf parameters  $\alpha_i$ ,  $\beta_i$  in the functional form (3.2). In that situation, it is the detected explicit form for  $\hat{h}(\xi, \eta)$  that is used in (4.7). The above approach offers several advantages, including the following:

1. SECB is a direct *noniterative* method that simultaneously restores information at all frequencies. Given the regularization parameters  $\epsilon$ ,  $M$ ,  $K$ , and  $s$ , SECB deblurring of a  $512 \times 512$  image requires about 4 seconds of CPU time on an SGI R10000. In contrast, many probabilistic methods often require thousands of iterations, and several hours of CPU time, to reconstruct the same amount of detail that is possible with the SECB method. See [6].

2. With  $H^t$  as in (3.3), and  $f^\dagger$  as in (4.7), one can form and display

$$(4.8) \quad u^\dagger(x, y, t) = H^t f^\dagger(x, y)$$

for selected *decreasing* values of  $t$  lying between 1 and 0. This simulates *marching backward in time* in (4.2) and allows *monitoring* the gradual deblurring of the image.

As  $t \downarrow 0$  the image  $u(x, y, t)$  becomes sharper. However, noise and other artifacts typically become more noticeable as  $t \downarrow 0$ . Gradual deblurring allows detection of features in the image before they become obscured by noise or ringing artifacts. In particular, as will be seen in Figures 13 and 15, marching backward in time is crucial in the *APEX method* for blind deconvolution.

3. It is frequently the case that the unknown sharp image is an easily recognizable object. In that situation, a priori knowledge of  $\epsilon, M, K, s$  is not essential, and SECB may be used interactively as follows. Set  $\epsilon/M = 0$  in (4.7) and fix a value of  $s$  in the range  $0.001 \leq s \leq 0.01$ . The sharpness parameter  $K$  is then the only unknown quantity in (4.7) and may be adjusted interactively so as to achieve optimal results. Useful values of  $K$  typically lie in the range  $0 < K < 10$ . Higher levels of noise dictate smaller values of  $K$ , and vice versa. Beginning with a small value of  $K$ , increasing  $K$  increases sharpness in the restored image, until a threshold value is reached. Further increase in  $K$  brings out noise which eventually obscures the image. The optimal value of  $K$  can usually be located in less than a dozen trials and in under 60 seconds of CPU time for a  $512 \times 512$  image. This version of the SECB procedure is the one used in all blind deblurring experiments discussed below.

4. The SECB constraint does not require differentiability of the unknown image  $f(x, y)$ . This is an important consideration in medical imaging and other contexts where edges and localized singularities in  $f$ , corresponding to tumors, microcalcifications, and the like, need to be detected. By contrast, in the case of Tikhonov's method bounds must be placed on derivatives of  $f$  in order to stabilize the inversion and obtain error estimates [5], [6]. Such smoothness constraints may foreclose the detection of singularities. In the SECB method, there holds a rigorous  $L^2$  error bound  $\|f_e - f^\dagger\| \leq \sqrt{3} \Gamma \epsilon$ , where, for a fixed noise level  $\epsilon > 0$ , the computable constant  $\Gamma$  satisfies  $\Gamma \ll M/\epsilon$  provided  $s/s^* \gg 1$ .

5. The SECB constraint has recently been shown to play a fundamental role in a class of ill-posed partial differential equations, linear and nonlinear, that is considerably wider than (4.2). See [7]. This class includes the Navier–Stokes equations. For all of these problems, the SECB constraint results in error bounds for the reconstruction that are stronger than previously known error estimates.

**5. The class W of well-behaved images.** Let  $f_e(x, y)$  be the exact sharp image defined in (1.3). Since  $f_e(x, y) \geq 0$

$$(5.1) \quad |\hat{f}_e(\xi, \eta)| \leq \int_{R^2} f_e(x, y) dx dy = \hat{f}_e(0, 0) = \sigma > 0.$$

Also, since  $h(x, y) \otimes f_e(x, y) = g_e(x, y)$  and  $h(x, y)$  is a probability density,

$$(5.2) \quad \hat{g}_e(0, 0) = \int_{R^2} g_e(x, y) dx dy = \int_{R^2} f_e(x, y) dx dy = \hat{f}_e(0, 0) = \sigma > 0.$$

Using  $\sigma$  as a normalizing constant, we may normalize Fourier transform quantities  $\hat{q}(\xi, \eta)$  by dividing by  $\sigma$ . (In deblurring applications where  $g(x, y)$  is known while neither  $f_e(x, y)$  nor  $g_e(x, y)$  are known, we use  $\hat{g}(0, 0) \approx \hat{g}_e(0, 0)$  as the normalizing constant.) Let

$$(5.3) \quad \hat{q}^*(\xi, \eta) = \hat{q}(\xi, \eta)/\sigma$$

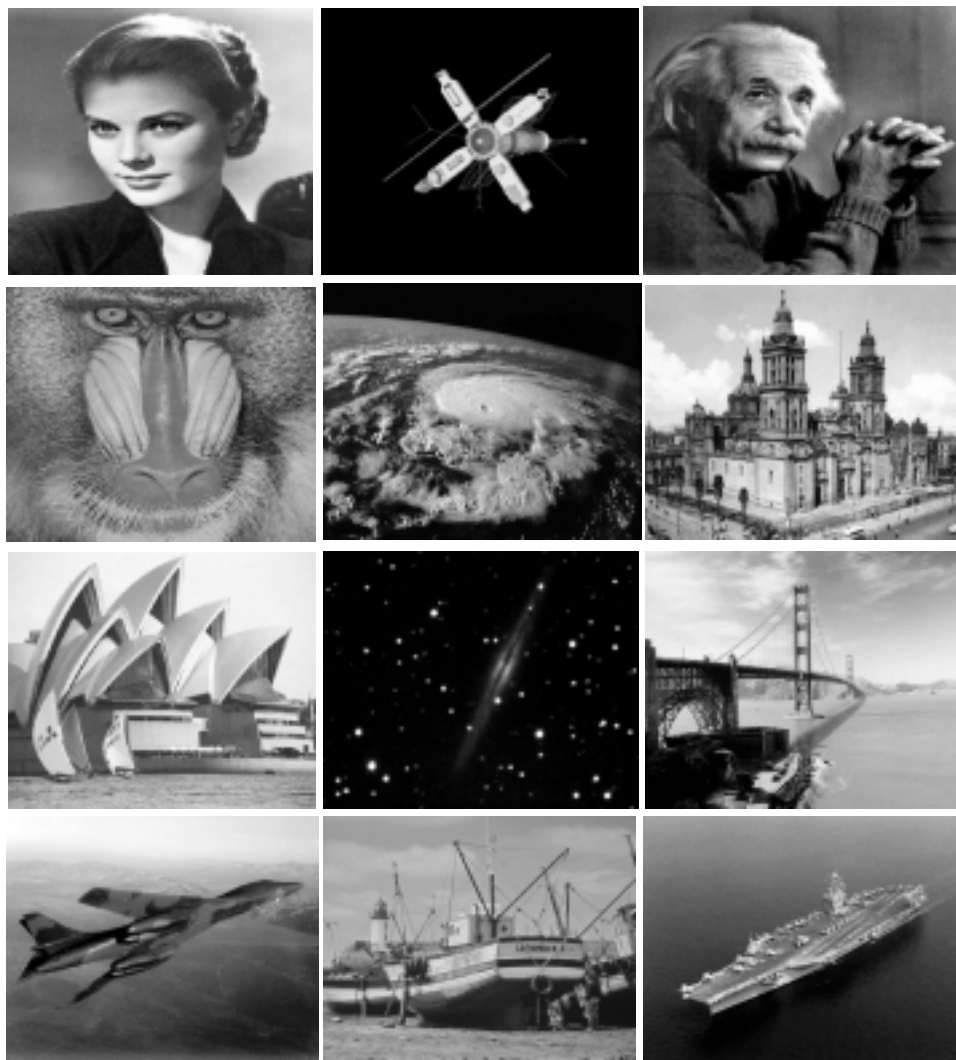
denote the normalized quantity. The function  $|\hat{f}_e^*(\xi, \eta)|$  is highly oscillatory, and  $0 \leq |\hat{f}_e^*| \leq 1$ . With  $r > 0$  and fixed  $\theta$ ,  $-\pi \leq \theta \leq \pi$ ,  $\xi = r \cos \theta$ ,  $\eta = r \sin \theta$ , let



FIG. 2. *Examples of images in class  $\mathbf{W}$ .*

$re^{i\theta}$  be a ray in the  $(\xi, \eta)$  plane. The two rays  $re^{i\theta}$ ,  $re^{i(\pi+\theta)}$  compose the line through the origin  $\eta = \xi \tan \theta$ . We shall be interested in the behavior of  $\hat{f}_e^*(\xi, \eta)$  along such rays and lines. Since  $f_e(x, y)$  is real, its Fourier transform is conjugate symmetric. Therefore the function  $|\hat{f}_e^*(\xi, \eta)|$  is symmetric about the origin on the line  $\eta = \xi \tan \theta$ . Since rotation of the image  $f_e(x, y)$  by an angle  $\phi$  rotates its Fourier transform by the same angle, behavior on the line  $\eta = \xi \tan \phi$  can be obtained by prerotating  $f_e(x, y)$  by the angle  $-\phi$  and examining its Fourier transform on the line  $\eta = 0$ .

Each of the 24 images in Figures 2 and 3 is a  $512 \times 512$  image quantized at 8-bits per pixel, i.e., each pixel value is an integer lying between 0 and 255. For the purposes of this discussion, each of these images is considered to be an exact sharp image  $f_e(x, y)$ . For each image, the discrete Fourier transform is a  $512 \times 512$  array of

FIG. 3. Further examples of images in class  $\mathbf{W}$ .

complex numbers, which we again denote by  $\hat{f}_e(\xi, \eta)$  for simplicity. The “frequencies”  $\xi, \eta$  are now integers lying between  $-256$  and  $256$ , and the zero frequency is at the center of the transform array. This ordering is achieved by premultiplying  $f_e(x, y)$  by  $(-1)^{x+y}$ . The discrete transforms  $\hat{f}_e^*(\xi, 0)$ , and  $\hat{f}_e^*(0, \eta)$  are immediately available. Image rotation may be used to obtain discrete transforms along other directions.

The collection of images in Figures 2 and 3 includes several standard images used as test objects in the image-analysis literature. It is an interesting observation that these diverse images have a great deal in common, namely the behavior of  $\log |\hat{f}_e^*(\xi, \eta)|$  along lines  $\eta = \xi \tan \theta$  in the  $(\xi, \eta)$  plane. The behavior in the first image in Figure 3 (Grace Kelly) is typical. In Figure 4(A),  $\log |\hat{f}_e^*(\xi, 0)|$  is plotted for Grace Kelly. While local behavior is highly oscillatory, the global behavior is roughly monotone decreasing as  $|\xi|$  increases. Indeed, on  $0 \leq \xi \leq 256$ , a least squares fit

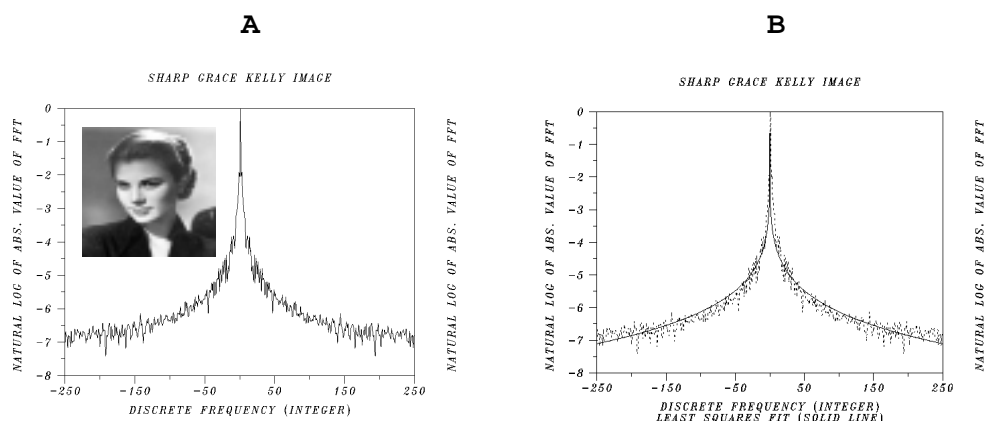


FIG. 4. (A)  $\log |\hat{f}_e^*(\xi, 0)|$  in discrete Fourier transform of sharp Grace Kelly image. (B) Least squares fit with function  $v(\xi) = -2.92 |\xi|^{0.1612}$  (solid line).

to the data with an appropriate *convex* monotone decreasing function provides a fair representation of gross data behavior. This is the case with  $v(\xi) = -2.92 \xi^{0.1612}$ , for example, as shown in Figure 4(B). Similar results are found along other rays  $re^{i\theta}$ . Moreover, while the rate of decay varies with direction, no direction seems to exist in which decay is dramatically faster than in other directions. For each of these 24 images, a limited search along several random directions reveals the same pattern of global monotone decay in  $\log |\hat{f}_e^*(\xi, \eta)|$ . And, while images with many edges tend to decay more slowly, the rate of decay is roughly of the same general order of magnitude for all these images. Noticeably absent are lines  $\eta = \xi \tan \theta$  where  $|\hat{f}_e^*(\xi, \eta)|$  vanishes on an interval or where  $\log |\hat{f}_e^*(\xi, \eta)|$  suddenly undergoes a large change in its range of values, remaining in the new range of values over an extended frequency interval. In Figure 4(B) and elsewhere in this paper, nonlinear least squares algorithms were used to fit the data with the assumed model  $v(\xi) = -a |\xi|^b$ ,  $a, b > 0$ . The nonlinear procedure returns the values of  $a$  and  $b$ . A most effective interactive framework for performing such least squares fitting is the *fit* command in *Dataplot* [16], a high-level English-syntax graphics and analysis software package developed at the National Institute of Standards and Technology. This software tool was used throughout this paper.

It should be noted that the process of 8-bit *rounding* used to create digitized images introduces a certain amount of noise. The intensity level of this background noise typically precludes actual zero values in the discrete Fourier transform of a digitized image. This may be verified experimentally as follows. In the 2-D FFT of Grace Kelly, set equal to zero all components  $\hat{f}_e(\xi, \eta)$  for which the integer frequencies  $\xi, \eta$  satisfy  $25 \leq \xi^2 + \eta^2 \leq 12100$ . If this modified  $512 \times 512$  array is inverse transformed and all pixel values rounded to 8-bits, a new image  $f_p(x, y)$  is created, with integer pixel values between 0 and 255. This perturbed image is neither sharp nor recognizable. However, while  $\log |\hat{f}_p^*(\xi, 0)|$  deviates strongly from the behavior shown in Figure 4(A), noise in  $f_p(x, y)$  prevents actual zero values in  $\hat{f}_p(\xi, \eta)$ .

These considerations indicate that a wide variety of sharp digitized images  $f_e(x, y)$  apparently belong to the class **W** defined as follows:

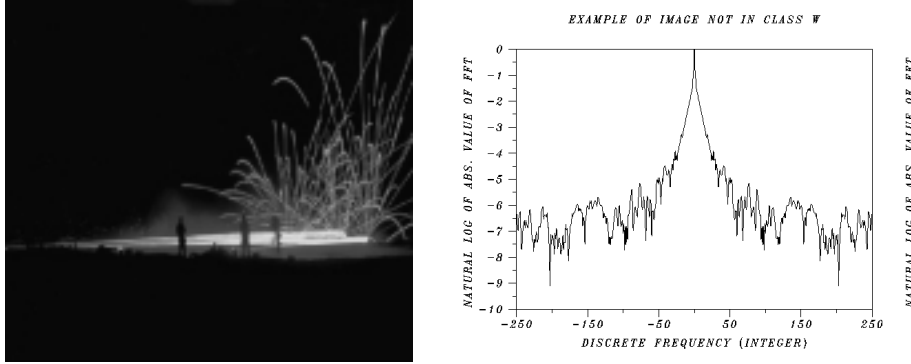


FIG. 5. Sharp image not in class **W** because  $\log |\hat{f}_e^*(\xi, 0)|$  is not globally monotone.

- $|\hat{f}_e^*(\xi, \eta)|$  has at most isolated zeros in the  $(\xi, \eta)$  plane.
- Neglecting isolated singularities, the global behavior of  $\log |\hat{f}_e^*(\xi, \eta)|$  on any ray  $re^{i\theta}$  is monotone decreasing with increasing  $r$ ; i.e., on the ray  $re^{i\theta}$ , a least squares fit to  $\log |\hat{f}_e^*(\xi, \eta)|$  with an appropriate monotone decreasing function provides a fair representation of gross data behavior as  $r$  increases.
- While the rate of decay may vary between rays, this decay is relatively slow, i.e., of a general order of magnitude comparable to that found in the sharp Grace Kelly image.

Not all digitized sharp images are in class **W**. An interesting sharp image not in **W** is shown in Figure 5.

**6. Blurring, rounding, and noise in the Fourier domain.** The psf detection techniques discussed in this paper involve the behavior of the blurred image along a single ray in the Fourier transform plane. The subsequent deconvolution procedure is also Fourier based. Accordingly, it is necessary to understand the effects of blurring and noise in the Fourier domain. This may be illustrated with a known sharp image. The  $512 \times 512$  MRI brain image  $f_e(x, y)$  (first image in Figure 2) was blurred computationally by multiplying the discrete Fourier transform of  $f_e(x, y)$  with the discrete Fourier transform of a Cauchy density simulating X-ray scattering. A double precision calculation was used to form

$$(6.1) \quad \hat{g}(\xi, \eta) = \hat{f}_e(\xi, \eta) e^{-0.075(\xi^2 + \eta^2)^{1/2}},$$

where  $\xi, \eta$  are integer frequencies and  $-256 \leq \xi, \eta \leq 256$ . The inverse transform of  $\hat{g}(\xi, \eta)$  when calculated and stored in 64-bit precision will be considered to be the noiseless blurred image  $g_e(x, y)$ . We need to distinguish that image from the usual 8-bit rounded blurred image  $g_s(x, y)$ , even though these two images are visually indistinguishable.

While 8-bit rounding noise in  $g_s(x, y)$  is invisible, it plays a crucial role in deconvolution as will become abundantly clear. However, blurred images are sometimes corrupted by additional noise processes. For illustration, a significant amount of Poisson noise was added to  $g_s(x, y)$  as follows. At each pixel location in  $g_s(x, y)$ , the corresponding integer gray-level value  $k$  was viewed as the mean value of a Poisson distribution. Using a Poisson random number generator with mean  $k$ , a Poisson deviate  $l$  was obtained. The pixel value  $k$  was then replaced by  $l$ . This procedure was

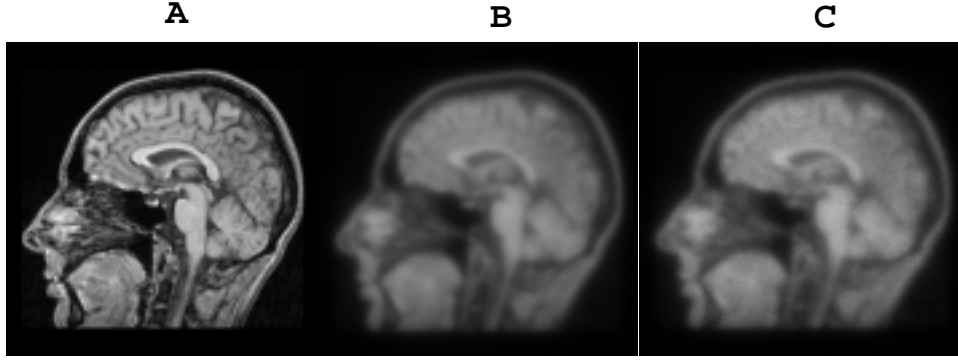


FIG. 6. Effects of blurring and noise in MRI brain image. (A) Sharp MRI brain image  $f_e(x, y)$ . (B) Cauchy blurred MRI image  $g_8(x, y)$  stored in 8-bit precision. (C) Image  $g_p(x, y)$  obtained by adding Poisson noise to image (B).

repeated for each pixel in turn, resulting in independent Poisson processes at each pixel location. Because the variance of a Poisson distribution is equal to its mean, relatively large deviations are possible. As a result, one can expect to visually distinguish the Poisson noised image  $g_p(x, y)$  from  $g_8(x, y)$ . This is indeed the case. The sharp MRI image  $f_e(x, y)$ , the 8-bit rounded Cauchy blurred image  $g_8(x, y)$ , and the Poisson noised Cauchy blurred image  $g_p(x, y)$  are shown in Figure 6.

In Fourier space, using the normalization (5.3) and with  $n_8(x, y)$  and  $n_p(x, y)$ , respectively, denoting 8-bit and Poisson noise, we have

$$\begin{aligned} \hat{g}_e^*(\xi, \eta) &= \hat{f}_e^*(\xi, \eta) e^{-0.075(\xi^2 + \eta^2)^{1/2}}, \\ (6.2) \quad \hat{g}_8^*(\xi, \eta) &= \hat{g}_e^*(\xi, \eta) + \hat{n}_8^*(\xi, \eta), \\ \hat{g}_p^*(\xi, \eta) &= \hat{g}_8^*(\xi, \eta) + \hat{n}_p^*(\xi, \eta). \end{aligned}$$

Hence,

$$(6.3) \quad \log |\hat{g}_e^*(\xi, 0)| = -0.075|\xi| + \log |\hat{f}_e^*(\xi, 0)|.$$

The plot of  $\log |\hat{f}_e^*(\xi, 0)|$  in Figure 7(A) displays the characteristic behavior of a class **W** image. The relatively slow decay in  $\log |\hat{f}_e^*(\xi, 0)|$  compared to that in  $-0.075|\xi|$  means that the global behavior in  $\log |\hat{g}_e^*(\xi, 0)|$  for large  $|\xi|$  is primarily that in  $-0.075|\xi|$ . As a result, the plot of  $\log |\hat{g}_e^*(\xi, 0)|$  in Figure 7(B) clearly reveals the signature of the Cauchy psf in the data  $g_e(x, y)$ .

Consider now  $\log |\hat{g}_8^*(\xi, 0)|$  in Figure 7(C). Here, global behavior reflects the fact that  $|\hat{g}_e^*(\xi, 0)| \ll |\hat{n}_8^*(\xi, 0)|$  for large  $|\xi|$ , as the negative exponential in the psf eventually drives  $|\hat{g}_e^*(\xi, 0)|$  below 8-bit noise level. Comparison with Figure 7(B) shows that high frequency behavior is undetectable in  $g_8(x, y)$ . That is why restoration of  $g_8(x, y)$ , even with exact knowledge of the psf, cannot recover  $f_e(x, y)$  exactly. This is true no matter which deblurring method is used. Nevertheless,  $|\hat{g}_e^*(\xi, 0)| \gg |\hat{n}_8^*(\xi, 0)|$  over a broad frequency range, and the psf signature is still visible in  $\log |\hat{g}_8^*(\xi, 0)|$ .

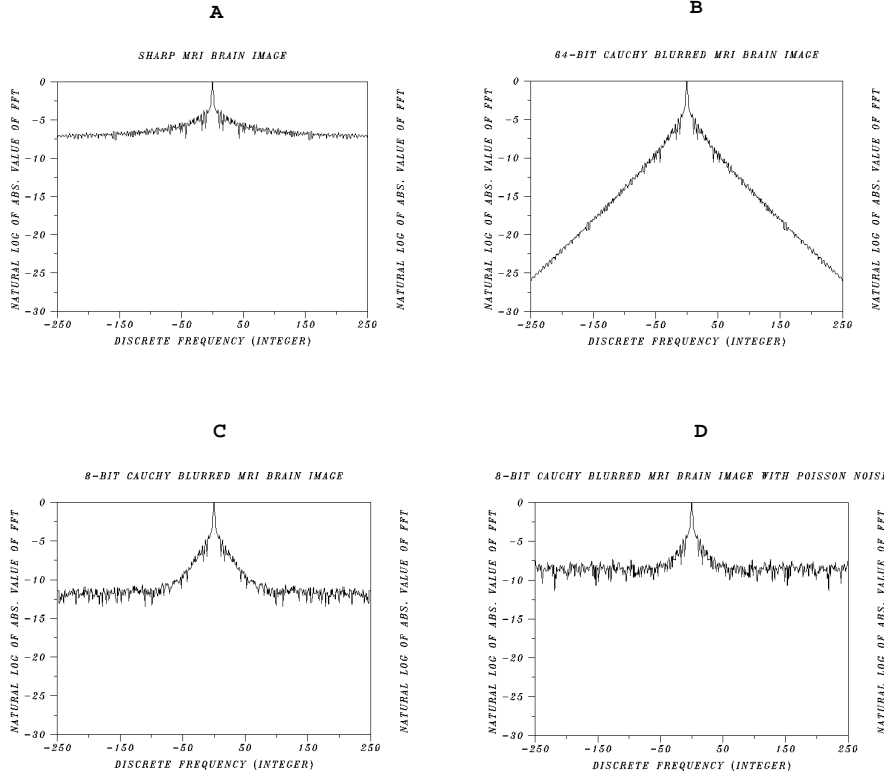


FIG. 7. Effects of blurring and noise in MRI brain image viewed along line  $\eta = 0$  in Fourier transform plane. (A)  $\log |\hat{f}_e^*(\xi, 0)|$  in sharp MRI brain image. (B)  $\log |\hat{g}_e^*(\xi, 0)|$  in blurred MRI image stored in 64-bit precision. (C)  $\log |\hat{g}_8^*(\xi, 0)|$  in blurred MRI image stored in 8-bit precision. (D)  $\log |\hat{g}_p^*(\xi, 0)|$  in Poisson noised blurred MRI image.

Indeed, we find

$$(6.4) \quad \log |\hat{g}_8^*(\xi, 0)| \approx \begin{cases} \log |\hat{g}_e^*(\xi, 0)|, & |\xi| \leq 50, \\ \log |\hat{n}_8^*(\xi, 0)|, & |\xi| \geq 75. \end{cases}$$

Evidently, because of 8-bit noise, any possible reconstruction of  $f_e(x, y)$  must be based on knowledge of  $\hat{g}_8(\xi, \eta)$  restricted to the disc  $0 \leq (\xi^2 + \eta^2)^{1/2} \leq 50$ . The situation is even worse in the Poisson noise case in Figure 7(D). The frequency range over which  $|\hat{g}_p^*(\xi, 0)| \gg |\hat{n}_p^*(\xi, 0)|$  is narrower, and the psf signature is barely visible in  $\log |\hat{g}_p^*(\xi, 0)|$ . This time, we find

$$(6.5) \quad \log |\hat{g}_p^*(\xi, 0)| \approx \begin{cases} \log |\hat{g}_e^*(\xi, 0)|, & |\xi| \leq 35, \\ \log |\hat{n}_p^*(\xi, 0)|, & |\xi| \geq 45. \end{cases}$$

Reconstruction of  $f_e(x, y)$  must now be based on knowledge of  $\hat{g}_p(\xi, \eta)$  restricted to the disc  $0 \leq (\xi^2 + \eta^2)^{1/2} \leq 35$ . Inevitably, such incomplete knowledge places serious limitations on the quality of the restoration that can be achieved. For this reason,

many new imaging devices record images in 16-bit or even 24-bit precision, and there is considerable interest in suppressing noise.

The above discussion sets the stage for development of our methods. Comparison of Figures 7(C) and 7(D) with Figure 7(B) will be used as a guide in visually determining an interval over which  $\log |\hat{g}^*(\xi, 0)|$  lies above noise level. Such an interval must exclude the regions where the gross behavior in  $\log |\hat{g}^*(\xi, 0)|$  can be well-approximated by a horizontal line. We now turn to the question of detecting the psf by examination of the noisy blurred image.

### 7. The BEAK method in psf identification from blurred image data.

As noted in section 2, a priori information on  $h(x, y)$  and  $f(x, y)$  is necessary to reduce the multiplicity of solutions in blind deconvolution. Nonnegativity and support constraints are the most common forms of a priori input, but they are not always effective and do not necessarily lead to well-behaved iterative algorithms. In this connection, the results in the present section are highly significant. We shall show that for class **W** images, knowledge of the gross behavior of  $\log |\hat{f}_e^*(\xi, \eta)|$  along a *single ray* in the Fourier transform plane is sufficient to approximately identify a class **G** psf from blurred image data along the *same ray*. By prerotating the image if necessary, we may assume that single ray or line to be the line  $\eta = 0$ . As in the case of the sharp Grace Kelly image in Figure 4(B), gross behavior along the line  $\eta = 0$  is *defined* to be the function  $v(\xi) = -a |\xi|^b$ ,  $a, b > 0$ , that provides the best least squares fit to  $\log |\hat{f}_e^*(\xi, 0)|$  on  $0 \leq |\xi| \leq 256$ . Therefore, this particular form of a priori input reduces to the two positive numbers  $a$  and  $b$ . The resulting psf identification is almost always surprising and must be understood in a broad sense. This method is termed the *BEAK method* for reasons to be explained below.

There are several practical situations where such a priori information may be available or may be estimated. For example, in blind deblurring of satellite images, a sharp image of a similar satellite might be used to estimate  $a$  and  $b$ . Likewise, the sharp MRI of a different patient, or the face of a different person, might provide useful values for  $a$  and  $b$ . See [8]. Consequently, while the theoretical significance of these results is stressed, the method is applicable in numerous contexts. In addition, the discussion serves to motivate the more generally applicable *APEX method* developed in section 8.

The BEAK method is based on the following observations (see Figure 7). In the basic relation

$$(7.1) \quad g(x, y) = h(x, y) \otimes f_e(x, y) + n(x, y),$$

we may safely assume that the noise  $n(x, y)$  satisfies

$$(7.2) \quad \int_{R^2} |n(x, y)| dx dy \ll \int_{R^2} f_e(x, y) dx dy = \sigma > 0,$$

so that

$$(7.3) \quad |\hat{n}^*(\xi, \eta)| \ll 1.$$

Consider the case where the psf is a pure Lévy density  $\hat{h}(\xi, \eta) = e^{-\alpha(\xi^2 + \eta^2)^\beta}$ . Since  $g = g_e + n$

$$(7.4) \quad \log |\hat{g}^*(\xi, \eta)| = \log |e^{-\alpha(\xi^2 + \eta^2)^\beta} \hat{f}_e^*(\xi, \eta) + \hat{n}^*(\xi, \eta)|.$$

Let  $\Omega = \{(\xi, \eta) \mid \xi^2 + \eta^2 \leq \omega^2\}$  be a neighborhood of the origin where

$$(7.5) \quad e^{-\alpha(\xi^2 + \eta^2)^\beta} |\hat{f}_e^*(\xi, \eta)| \gg |\hat{n}^*(\xi, \eta)|.$$

Such an  $\Omega$  exists since (7.5) is true for  $\xi = \eta = 0$  in view of (7.3). The radius  $\omega > 0$  of  $\Omega$  decreases as  $\alpha$  and  $n$  increase. For  $(\xi, \eta) \in \Omega$  we have

$$(7.6) \quad \log |\hat{g}^*(\xi, \eta)| \approx -\alpha(\xi^2 + \eta^2)^\beta + \log |\hat{f}_e^*(\xi, \eta)|.$$

Hence, for  $|\xi| \leq \omega$ ,

$$(7.7) \quad \log |\hat{g}^*(\xi, 0)| \approx -\alpha|\xi|^{2\beta} + \log |\hat{f}_e^*(\xi, 0)|.$$

The idea is to replace the unknown  $\log |\hat{f}_e^*(\xi, 0)|$  in (7.7) by its least squares approximation  $v(\xi) = -a|\xi|^b$ . The detection procedure is then the following. With  $a$  and  $b$  given a priori, find positive numbers  $\tilde{\alpha}$ ,  $\tilde{\beta}$ , so that the function  $u(\xi) = -\tilde{\alpha}|\xi|^{2\tilde{\beta}} - a|\xi|^b$  best fits  $\log |\hat{g}^*(\xi, 0)|$  on  $|\xi| \leq \omega$ . This may be accomplished interactively using nonlinear least squares algorithms in *Dataplot* [16]. The returned values for  $\tilde{\alpha}$  and  $\tilde{\beta}$  are subsequently used for  $\hat{h}(\xi, \eta)$  in the SECB deblurring procedure (4.7).

For more general class **G** psfs where  $\hat{h}(\xi, \eta) = e^{-\sum_{i=1}^N \alpha_i (\xi^2 + \eta^2)^{\beta_i}}$ , we again seek the best fit to  $\log |\hat{g}^*(\xi, 0)|$  on  $|\xi| \leq \omega$ , with a function  $u(\xi) = -\tilde{\alpha}|\xi|^{2\tilde{\beta}} - a|\xi|^b$ . Here, the returned values for  $\tilde{\alpha}$  and  $\tilde{\beta}$  may be considered average values for the  $\alpha_i$ ,  $\beta_i$ , and are expected to generate a pure Lévy density that well-approximates the composite psf.

We shall now demonstrate this technique by applying it to three examples. The first two examples involve the blurred MRI images discussed in the previous section. Recall that those images were blurred with a Cauchy density with  $\alpha = 0.075$  and  $\beta = 0.5$ . We first need to supply the a priori information  $a$ ,  $b$  characterizing the gross behavior of  $\log |\hat{f}_e^*(\xi, 0)|$ . Applying nonlinear least squares to the exact MRI image in Figure 6(A), we find that the best fit to  $\log |\hat{f}_e^*(\xi, 0)|$  with a function of the form  $v(\xi) = -a|\xi|^b$ ,  $a, b > 0$ , on  $-256 \leq \xi \leq 256$  occurs when  $a = 3.117$  and  $b = 0.155$ . The result is shown in Figure 8(A).

For the 8-bit image  $g_8(x, y)$  in Figure 6(B), we now best-fit  $\log |\hat{g}_8^*(\xi, 0)|$  in Figure 7(C) with  $u(\xi) = -\alpha|\xi|^{2\beta} - 3.117|\xi|^{0.155}$ , on the interval  $-50 \leq \xi \leq 50$ , where the signal is clearly above noise level. This leads to  $\alpha = 0.05$ ,  $\beta = 0.557$ , and the result is shown in Figure 8(B). The returned values for  $\alpha$  and  $\beta$  differ from the correct values  $\alpha = 0.075$ ,  $\beta = 0.5$  that were used to construct Figure 6(B). However, interestingly, the point spread function with these incorrect values turns out to be *approximately equivalent* to the correct Cauchy psf, a phenomenon previously discussed in section 3.1 and illustrated in Figure 1(B). In the Poisson noised image  $g_p(x, y)$  in Figure 6(C), the same procedure is now applied to  $\log |\hat{g}_p^*(\xi, 0)|$  in Figure 7(D), but on the substantially reduced interval  $-35 \leq \xi \leq 35$ . This time, we get  $\alpha = 0.03$ ,  $\beta = 0.636$ , and the result is shown in Figure 8(C). Surprisingly, this detected psf is again approximately equivalent to the correct Cauchy psf! The two detected psfs, together with the exact psf, are plotted in Figure 8(D).

As noted in Figures 7(C) and 7(D) and the discussion in section 6, only a part of the information necessary to reconstruct  $f_e(x, y)$  is available in the blurred image data  $g(x, y)$ . Consequently, even when the exact psf is known, the quality of this reconstruction is necessarily limited, no matter which restoration algorithm is used. From this standpoint, applying the SECB method with these two detected psfs results



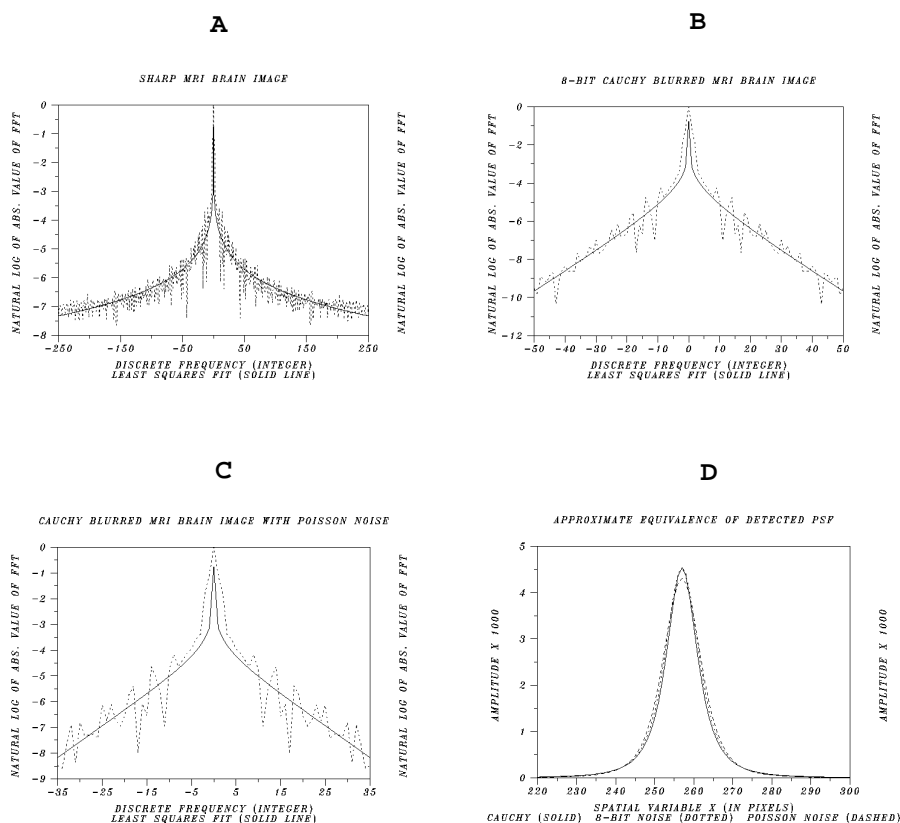


FIG. 8. BEAK method of psf detection in noisy blurred MRI brain image when gross behavior of  $\log |\hat{f}_e^*(\xi, 0)|$  is known. (A) Least squares fit of  $\log |\hat{f}_e^*(\xi, 0)|$  in sharp MRI image with  $v(\xi) = -3.117 |\xi|^{0.155}$ ,  $-256 \leq \xi \leq 256$  (solid line). (B) Least squares fit of  $\log |\hat{g}_s^*(\xi, 0)|$  in 8-bit blurred image, with  $u(\xi) = -\alpha |\xi|^{2\beta} + v(\xi)$ ,  $-50 \leq \xi \leq 50$  (solid line), returns detected parameters  $\alpha = 0.05$ ,  $\beta = 0.557$ . (C) Least squares fit of  $\log |\hat{g}_p^*(\xi, 0)|$  in Poisson noised image with above  $u(\xi)$  on  $-35 \leq \xi \leq 35$  (solid line) returns detected parameters  $\alpha = 0.03$ ,  $\beta = 0.636$ . (D) Detected psfs approximately equivalent to original Cauchy psf with  $\alpha = 0.075$ ,  $\beta = 0.5$ .

in quite sound restorations, as shown in Figure 9. In [6], a variety of linear and nonlinear deblurring methods are applied to these same blurred MRI images, with *exact knowledge* of the blurring Cauchy psf. The restorations in Figure 9 are of a quality comparable to those obtained in [6]. It is significant that the presence of heavy Poisson noise in Figure 6(C) did not preclude detection of a point spread function closely approximating the true psf.

The last example involves the satellite image (second image in Figure 3), blurred with a Lévy density with  $\alpha = 0.015$ ,  $\beta = 0.925$ , and 8-bit rounding noise. Here, the blurring is more severe than in Figure 9(A). As a result,  $\log |\hat{g}^*(\xi, 0)|$  in Figure 10(B) is visually determined to lie above noise level only on the small interval  $0 \leq |\xi| \leq 25$ . At the same time, a least squares fit to  $\log |\hat{f}_e^*(\xi, 0)|$  with  $v(\xi) = -a |\xi|^b$  returns  $a = 1.99$  and  $b = 0.255$ , but produces a relatively poor fit as shown in Figure 10(A). Consequently, the a priori information  $a = 1.99$ ,  $b = 0.255$  does *not* accurately portray the gross behavior in  $\log |\hat{f}_e^*(\xi, 0)|$ . Using that a priori information, we now best-fit

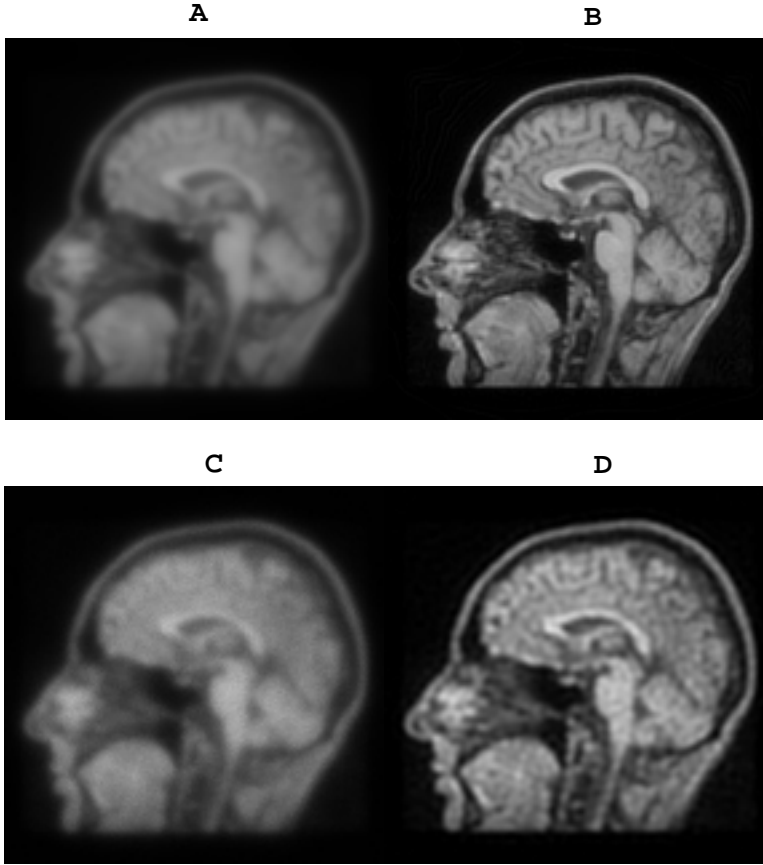


FIG. 9. *Blind deblurring experiment with noisy data.* (A) Blurred MRI image with  $\alpha = 0.075$ ,  $\beta = 0.5$ , stored in 8-bit precision. (B) SECB deblurring of image (A) using  $s = 0.001$ ,  $K = 0.8$ , and BEAK detected psf parameters  $\alpha = 0.05$ ,  $\beta = 0.557$ , obtained by least squares fit in Figure 8(B). (C) Image (A) with added Poisson noise. (D) SECB deblurring of image (C) using  $s = 0.001$ ,  $K = 0.035$ , and BEAK detected psf parameters  $\alpha = 0.03$ ,  $\beta = 0.636$ , obtained by least squares fit in Figure 8(C).

$\log |\hat{g}^*(\xi, 0)|$  on  $0 \leq |\xi| \leq 25$ , with  $u(\xi) = -\alpha |\xi|^{2\beta} - 1.99 |\xi|^{0.255}$ . This leads to  $\alpha = 0.0433$ ,  $\beta = 0.752$ , and the result is shown in Figure 10(C). As indicated in Figure 10(D), the detected psf is not equivalent to the true psf. Nevertheless, using that detected psf in the SECB method with  $s = 0.001$  and  $K = 0.8$  produces a very good restoration, as shown in Figure 11.

The behavior of the above psf detection method in the MRI and satellite images, as described in Figures 8 through 11, is representative of the class **W**. Numerous blind deblurring experiments on the universe consisting of the 24 images in Figures 2 and 3, blurred with a large variety of class **G** psfs, and in the presence of various kinds of added noise, produce similar results. (The “beak” shape of the fitted curve near  $\xi = 0$  in Figures 8(B), 8(C), and 9(C) suggested the terminology BEAK method.) Often, the detected psf is found to be approximately equivalent to the true psf. This may happen with as much as 10% added noise. At other times, the detected psf overshoots (or undershoots) the true psf by small amounts, and is correspondingly slightly narrower (or wider) than the true psf. In almost all cases, however, the

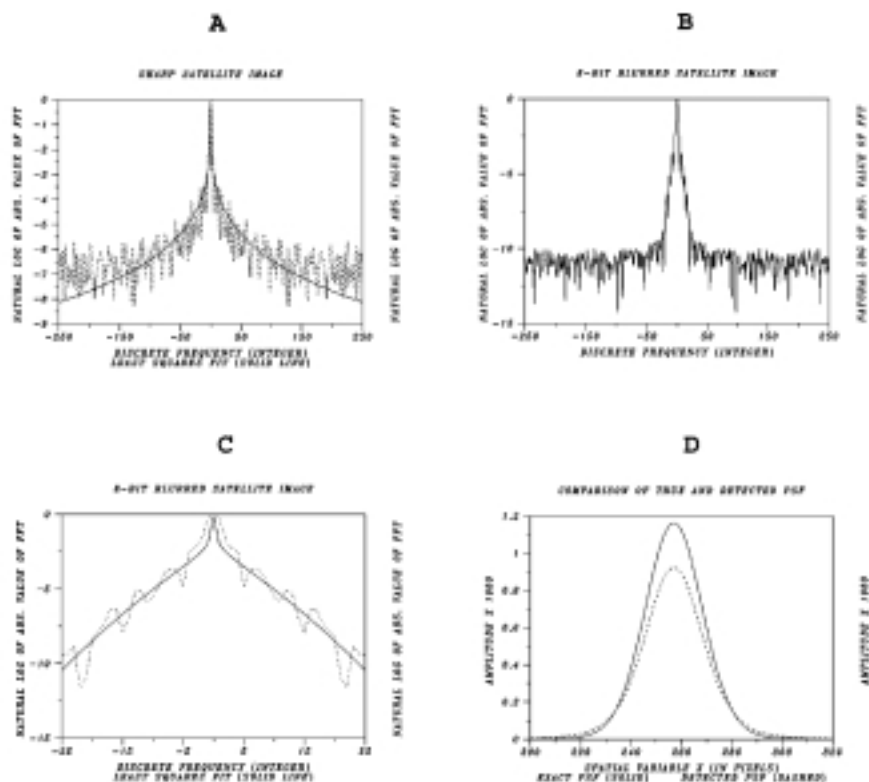


FIG. 10. BEAK method of psf detection in blurred satellite image when gross behavior of  $\log|\hat{f}_e^*(\xi, 0)|$  is known. (A) Least squares fit of  $\log|\hat{f}_e^*(\xi, 0)|$  in sharp satellite image with  $v(\xi) = -1.99|\xi|^{0.255}$  on  $-256 \leq \xi \leq 256$  (solid line) produces relatively poor fit. (B)  $\log|\hat{g}^*(\xi, 0)|$  in 8-bit blurred satellite image when psf is Lévy density with  $\alpha = 0.015$ ,  $\beta = 0.925$ . Trace lies above 8-bit noise level only on small interval,  $-25 \leq \xi \leq 25$ . (C) Least squares fit of  $\log|\hat{g}^*(\xi, 0)|$  with  $u(\xi) = -\alpha|\xi|^{2\beta} + v(\xi)$ ,  $-25 \leq \xi \leq 25$  (solid line), returns detected parameters  $\alpha = 0.0433$ ,  $\beta = 0.752$ . (D) Detected psf not equivalent to original psf.

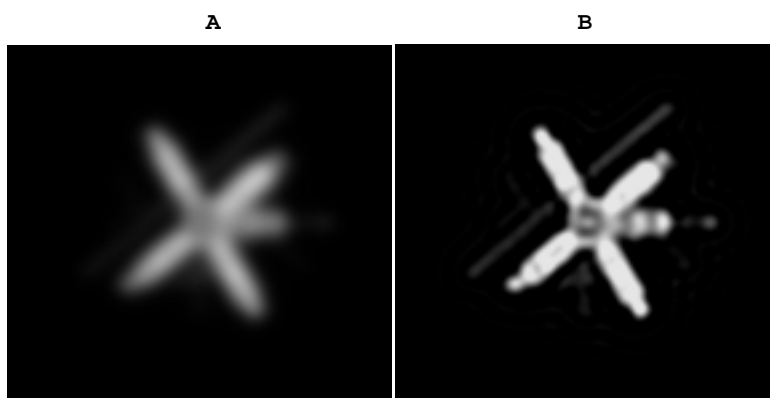


FIG. 11. Blind deblurring in 8-bit blurred satellite image. (A) Blurred image with  $\alpha = 0.015$ ,  $\beta = 0.925$ , stored in 8-bit precision. (B) SECB deblurring of image (A) using  $s = 0.001$ ,  $K = 0.8$ , and BEAK detected psf parameters  $\alpha = 0.0433$ ,  $\beta = 0.752$ , obtained by least squares fit in Figure 10(C). Good restoration achieved even though detected psf not equivalent to original psf.

detected psf together with the SECB algorithm produce useful restorations. On the other hand, as is evident from Figures 7(D) and 10(B), if the blur is too severe and/or the level of added noise is too high, the interval  $0 \leq |\xi| \leq \omega$  wherein the signal lies above noise becomes too small for detection of a useful psf. However, in such cases, useful restorations typically cannot be obtained even with exact knowledge of the true psf.

Extensive numerical experimentation using the BEAK method leads to the following conclusions.

- The idea of replacing the unknown  $\log |\hat{f}_e^*(\xi, 0)|$  in (7.7) with its gross behavior  $v(\xi) = -a|\xi|^b$  is plausible and demonstrably useful. Evidently, for class **W** images, local fluctuations in the exact image Fourier transform are not important in detecting the parameters of a class **G** psf from blurred image data. Only the large-scale behavior, summarized by the two positive numbers  $a$  and  $b$ , is significant.
- Detection and restoration are separate tasks, and each involves direct noniterative procedures based on FFT algorithms. The restoration phase generally requires interactive fine-tuning of the regularization parameters. However, for a  $512 \times 512$  image, each trial restoration requires about 5 seconds of CPU time on current desktop workstations. The detection phase likewise requires no more than a few seconds of CPU time.

**8. The APEX method and marching backward in time.** This method seeks to identify an approximate psf by examining blurred image data along a single ray in Fourier space, *without* prior knowledge of the gross behavior in  $\log |\hat{f}_e^*(\xi, 0)|$ . The method typically requires several interactive trials before locating a suitable candidate psf. As previously noted, such trial SECB restorations are easily obtained. In addition, by using the *marching backward in time* option in the SECB method, the APEX method becomes a robust and effective blind deconvolution tool. An unexpected result is that the APEX method can produce several distinct psfs leading to good restorations. In particular, a useful restoration may be obtained with a psf different from the one that originally blurred the image. On reflection, such nonuniqueness is not surprising since, in contrast to section 7, no a priori information regarding the sharp image is provided in the APEX method.

Let the true system psf be a pure Lévy density  $\hat{h}(\xi, \eta) = e^{-\alpha(\xi^2 + \eta^2)^\beta}$  and let  $\Omega$  be the neighborhood of the origin in Fourier space defined in (7.5). As in (7.7)

$$(8.1) \quad \log |\hat{g}^*(\xi, 0)| \approx -\alpha|\xi|^{2\beta} + \log |\hat{f}_e^*(\xi, 0)|, \quad 0 \leq |\xi| \leq \omega.$$

As shown in section 7, replacing  $\log |\hat{f}_e^*(\xi, 0)|$  in (8.1) by its least squares approximation  $v(\xi) = -a|\xi|^b$  allows for a reasonably representative fit to  $\log |\hat{g}^*(\xi, 0)|$  on the whole interval  $0 \leq |\xi| \leq \omega$ . In particular, the *beak* or *nib* in the fitted curve near  $\xi = 0$ , so evident in Figures 8(B), 8(C), and 9(C), follows directly from use of this prior knowledge. Providing for correct development of the *beak* in the least squares fit is essential to recovering pairs  $(\alpha, \beta)$  that produce approximately equivalent psfs.

In the absence of any knowledge regarding  $\log |\hat{f}_e^*(\xi, 0)|$ , we consider replacing it by a negative constant  $-A$  in (8.1). For any  $A > 0$ , the approximation

$$(8.2) \quad \log |\hat{g}^*(\xi, 0)| \approx -\alpha|\xi|^{2\beta} - A$$

is no longer valid near  $\xi = 0$ , since the curve  $u(\xi) = -\alpha|\xi|^{2\beta} - A$  has  $-A$  as its apex. The APEX method is based on the *expectation* that a value  $A_0 > 0$  can

be found such that away from the origin, the least squares fit of  $\log |\hat{g}^*(\xi, 0)|$  with  $u(\xi) = -\alpha|\xi|^{2\beta} - A_0$  conforms with the least squares fit that would have been obtained had the information necessary to form the *beak* near  $\xi = 0$  been available.

Choosing a value of  $A > 0$ , we best fit  $\log |\hat{g}^*(\xi, 0)|$  with  $u(\xi) = -\alpha|\xi|^{2\beta} - A$  on the interval  $0 \leq |\xi| \leq \omega$ , where the signal lies above noise level. The resulting fit is close only for  $\xi$  away from the origin. The returned values for  $\alpha$  and  $\beta$  are then used in the SECB deblurring algorithm. Different values of  $A$  return different pairs  $(\alpha, \beta)$  and the corresponding psfs are usually *not* approximately equivalent. Experience indicates that the optimal value of  $A$  generally lies in the interval  $2 \leq A \leq 6$ . Increasing the value of  $A$  decreases the curvature of  $u(\xi)$  at  $\xi = 0$ , resulting in a larger value of  $\beta$  together with a smaller value of  $\alpha$ . Decreasing  $A$  has the opposite effect. A value of  $A > 0$  that returns  $\beta > 1$  is clearly too large, as  $\beta > 1$  is impossible for probability density functions [13].

Assume the image  $g(x, y)$  was blurred with a Lévy density with parameters  $(\alpha_0, \beta_0)$ . A value of  $A$  that returns  $(\alpha_0, \beta_0)$  may not exist in general, but values of  $A$  that return pairs  $(\alpha, \beta)$  near  $(\alpha_0, \beta_0)$  do exist. If  $\alpha \approx \alpha_0$  while  $\beta > \beta_0$ , SECB deblurring with the pair  $(\alpha, \beta)$  overemphasizes high frequency components and typically produces graininess and/or noise in the deblurred image. One can reapply the SECB procedure with  $\beta$  reduced by a small amount while keeping  $\alpha$  at the same value. Another possibility is to decrease the value of  $A$  in the fitting procedure, obtaining a new pair  $(\alpha_1, \beta_1)$  with  $\alpha_1 > \alpha$ , and  $\beta_1 < \beta$ . If  $\alpha_1$  is too large, ringing artifacts usually appear in the deblurred image, and the SECB procedure is reapplied with a smaller  $\alpha_1$ . In this way, one can generally find several pairs  $(\alpha, \beta)$  that produce good restorations.

For more general class **G** psfs where  $\hat{h}(\xi, \eta) = e^{-\sum_{i=1}^J \alpha_i (\xi^2 + \eta^2)^{\beta_i}}$ , we may still use the approximation  $\log |\hat{g}^*(\xi, 0)| \approx -\alpha|\xi|^{2\beta} - A$ , and apply the same technique to extract a suitable pair  $(\alpha, \beta)$  from the blurred image. In this case, a single pure Lévy psf is being used to deblur an image that was originally blurred by a composite of such psfs.

Considerable *robustness* and flexibility are added to the APEX method by using the SECB *marching backward in time* option described in (4.8). In particular, it is not always necessary to locate a value of  $A$  that returns a pair  $(\alpha, \beta)$  near the correct values  $(\alpha_0, \beta_0)$  in order to obtain useful restorations. If  $\beta < \beta_0$  and  $\alpha > \alpha_0$ , and severe ringing results from SECB, this may be interpreted as having traveled *too far* in the backward solution of (4.2). By displaying the solution  $u^\dagger(x, y, t)$  in (4.8) for selected decreasing values of  $t$  lying between 1 and 0, one can monitor the gradual deblurring of the image. One can then locate a value  $t_0 > 0$  where substantial deblurring has occurred, but without the ringing and other artifacts that are present at  $t = 0$ . The image  $u^\dagger(x, y, t_0)$  is a useful restoration, but one that is typically of a different visual quality than would have been obtained at  $t = 0$ , using the correct pair  $(\alpha_0, \beta_0)$ . In some cases, however, this procedure can lead to superior restorations.

The following examples illustrate the flexibility of the APEX method. The USS Nimitz image (last image in Figure 3) was blurred with a Gaussian density with  $\alpha = 0.001$ ,  $\beta = 1.0$ , and the blurred image  $g(x, y)$  was stored in 8-bit precision. From Figure 12(A),  $\log |\hat{g}^*(\xi, 0)|$  was visually determined to lie above noise level on the interval  $0 \leq |\xi| \leq 60$ . We now seek the best least squares fit on that interval with  $u(\xi) = -\alpha|\xi|^{2\beta} - A$ , with  $A > 0$  specified. When  $A = 4.3$ , we recover the correct values,  $\alpha = 0.001, \beta = 1.0$ , and the fit is shown in Figure 12(B). When  $A = 2.5$ , however, the least squares fit returns a false Cauchy psf with  $\alpha_1 = 0.1, \beta_1 = 0.5$ , as

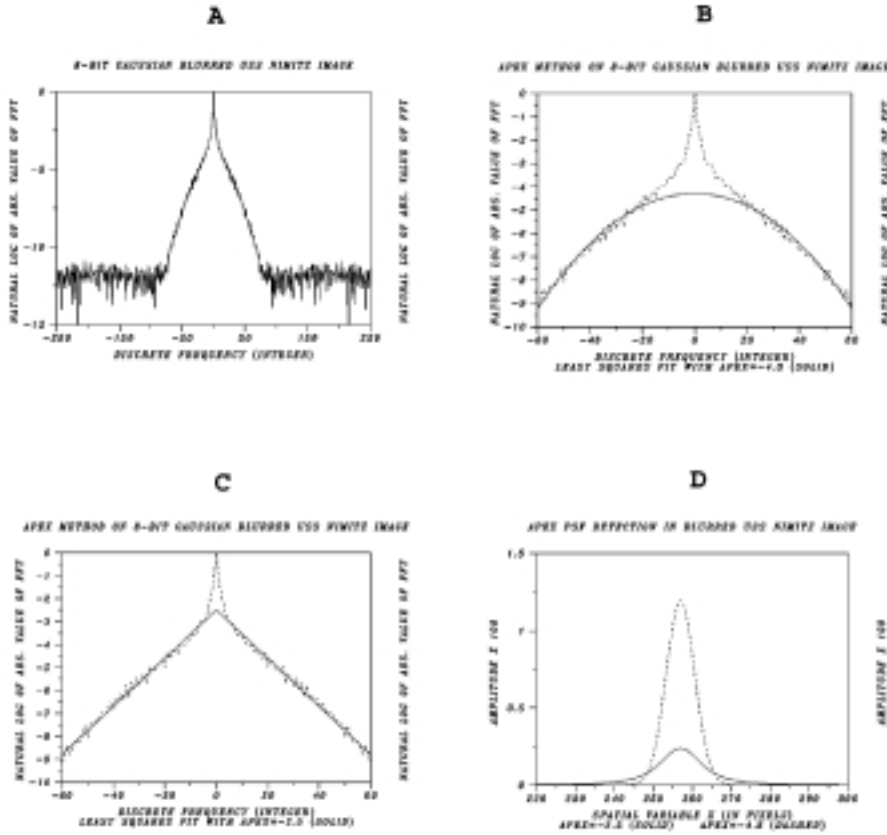


FIG. 12. APEX method of psf detection. (A)  $\log |\hat{g}^*(\xi, 0)|$  in Gaussian blurred USS Nimitz image with  $\alpha = 0.001$ ,  $\beta = 1.0$ , stored in 8-bit precision. Trace visually determined to lie above 8-bit noise level on interval  $-60 \leq \xi \leq 60$ . (B) Least squares fit of  $\log |\hat{g}^*(\xi, 0)|$  with  $u(\xi) = -\alpha |\xi|^{2\beta} - 4.3$  on  $-60 \leq \xi \leq 60$  (solid line) returns correct Gaussian psf with  $\alpha = 0.001$ ,  $\beta = 1.0$ . (C) Least squares fit of  $\log |\hat{g}^*(\xi, 0)|$  with  $u(\xi) = -\alpha |\xi|^{2\beta} - 2.5$  on  $-60 \leq \xi \leq 60$  (solid line) returns false Cauchy psf with  $\alpha = 0.1$ ,  $\beta = 0.5$ . (D) Cauchy psf (solid line) differs substantially from true Gaussian psf (dashed line).

shown in Figure 12(C). Note that  $\alpha_1 = 100 \alpha$ , and  $\beta_1 = 0.5 \beta$  so that the pair  $(\alpha_1, \beta_1)$  is not near  $(\alpha, \beta)$ . As shown in Figure 12(D) the false Cauchy psf differs substantially from the correct Gaussian psf.

The results of SECB deblurring with these detected psfs is shown in Figure 13. A very good restoration is obtained in Figure 13(B) using the correctly identified Gaussian psf, while the false Cauchy psf produces severe ringing in Figure 13(C). However, if backward in time continuation with the false psf is terminated at  $t = 0.45$  rather than at  $t = 0$ , a useful restoration ensues as shown in Figure 13(D). Clearly, the image in Figure 13(B) is sharper than that in Figure 13(D), but the latter is quite remarkable considering that  $\alpha_1 = 100 \alpha$ .

In the next example, the Golden Gate Bridge image in Figure 3 was blurred with a Lévy density with  $\alpha = 0.009$ ,  $\beta = 0.75$  and stored in 8-bit precision. The trace of  $\log |\hat{g}^*(\xi, 0)|$  in Figure 14(A) was visually determined to lie above noise level on the interval  $0 \leq |\xi| \leq 55$ . With  $A = 5.75$ , the APEX method returns approximately

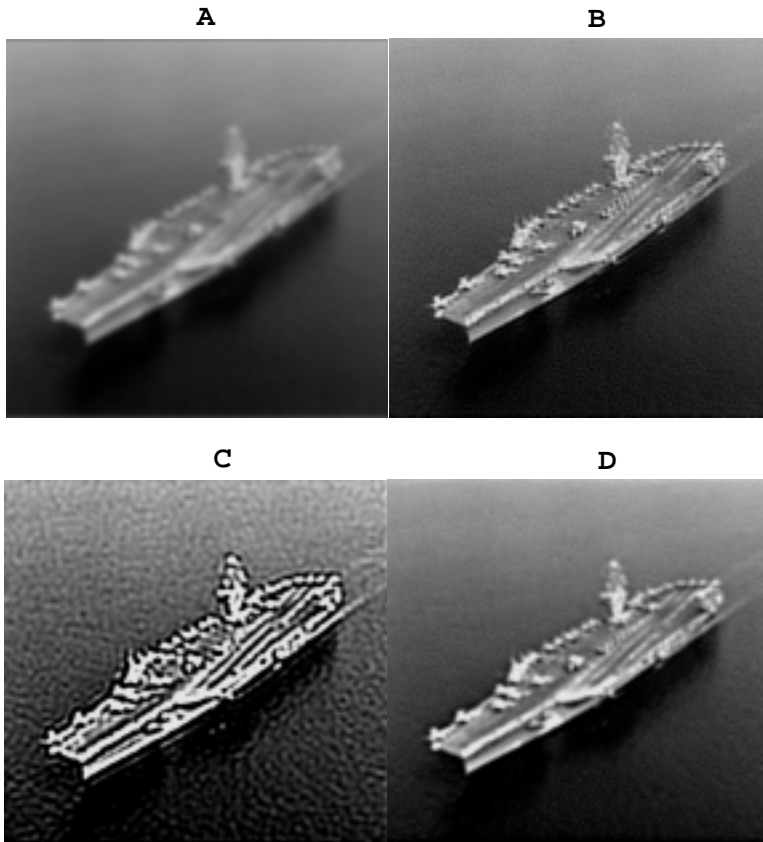


FIG. 13. APEX method in blind deblurring of Gaussian blurred Nimitz image. (A) Blurred image with  $\alpha = 0.001$ ,  $\beta = 1.0$ , stored in 8-bit precision. (B) SECB deblurring of image (A) using  $s = 0.001$ ,  $K = 0.65$ , and detected psf parameters  $\alpha = 0.001$ ,  $\beta = 1.0$  obtained by least squares fit in Figure 12(B) with apex = -4.3. (C) SECB deblurring of image (A) using  $s = 0.001$ ,  $K = 0.65$ , and false Cauchy psf with  $\alpha = 0.1$ ,  $\beta = 0.5$  obtained by least squares fit in Figure 12(C) with apex = -2.5. Wrong psf produces severe ringing. (D) SECB deblurring with false Cauchy psf as in (C), but with "marching backward in time" process in (4.8) terminated at  $t = 0.45$ . (Image (C) corresponds to  $t = 0$ .) Image (D) not as sharp as image (B).

correct values  $\alpha_1 = 0.01$ ,  $\beta_1 = 0.769$ , and the fit is shown in Figure 14(B). With  $A = 3.5$ , the curvature at the fit apex in Figure 14(C) is considerably greater than it is in Figure 14(B). The attempt to accommodate  $\log |\hat{g}^*(\xi, 0)|$  near  $\xi = 0$  without forming a *beak* results in erroneous values  $\alpha_2 = 0.332 \approx 37 \alpha$ ,  $\beta_2 = 0.378 \approx 0.5 \beta$ . These two detected psfs, shown in Figure 14(D), are substantially different. SECB deblurring with the approximately correct pair  $(\alpha_1, \beta_1)$  is shown in Figure 15(B). Deblurring with  $(\alpha_2, \beta_2)$  results in severe ringing, as shown in Figure 15(C). However, when backward in time continuation is terminated at  $t = 0.5$  rather than at  $t = 0$ , the image in Figure 15(D) is obtained. Overall, the image quality in Figure 15(D) is superior to that in Figure 15(B).

While both the APEX method and the BEAK method in section 7 can be successfully applied in the presence of noise, it should be recognized that noise affects both detection and deblurring phases. In the detection phase, the interval  $|\xi| \leq \omega$  may become too narrow to enable easy detection of pairs  $(\alpha, \beta)$  that produce good

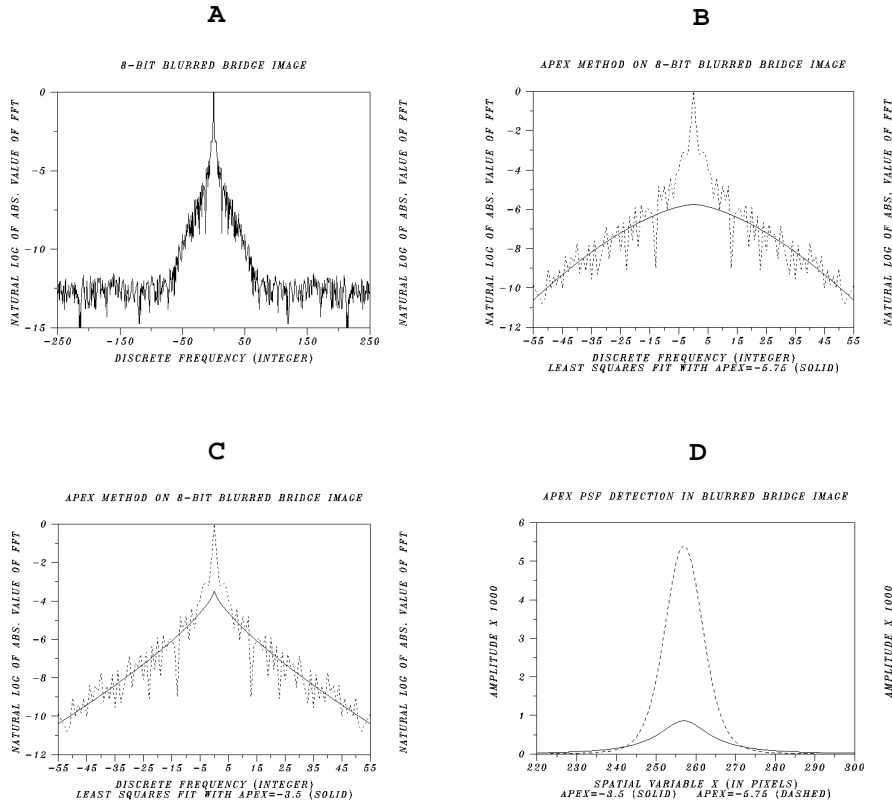


FIG. 14. APEX method of psf detection. (A)  $\log |\hat{g}^*(\xi, 0)|$  in blurred Golden Gate Bridge image with  $\alpha = 0.009$ ,  $\beta = 0.75$  stored in 8-bit precision. Trace visually determined to lie above 8-bit noise level on interval  $-55 \leq \xi \leq 55$ . (B) Least squares fit of  $\log |\hat{g}^*(\xi, 0)|$  with  $u(\xi) = -\alpha |\xi|^{2\beta} - 5.75$  on  $-55 \leq \xi \leq 55$  (solid line) returns approximately correct parameters  $\alpha = 0.01$ ,  $\beta = 0.769$ . (C) Least squares fit of  $\log |\hat{g}^*(\xi, 0)|$  with  $u(\xi) = -\alpha |\xi|^{2\beta} - 3.5$ ,  $-55 \leq \xi \leq 55$  (solid line), returns false parameters  $\alpha = 0.332$ ,  $\beta = 0.378$ . (D) False psf (solid line) differs substantially from approximate psf (dashed line).

restorations. Additional trial solutions may be necessary to locate an optimal pair. In the deblurring phase, as noted in Figure 7(D), noise masks high frequency information needed for high resolution reconstructions. This is reflected in lower values of  $K$  that must be used in the SECB method to control noise amplification. This limitation is independent of the detection phase, and is present even with *exact* knowledge of the psf.

The fact that detection and reconstruction are separate tasks provides a significant advantage over iterative blind deconvolution methods in the presence of noise. Iterative algorithms deblur the image at the  $n$ th stage using the psf calculated at the preceding stage. This deblurred image is then used to calculate a new psf. However, unexpected noise amplification in the deblurred image at any stage can seriously affect calculation of the psf at the next stage. Such errors propagate and may amplify as the iteration progresses. The close coupling of detection with restoration is one reason why the iterative approach is often ill-behaved.

It is instructive to examine the performance of the APEX method when the lim-



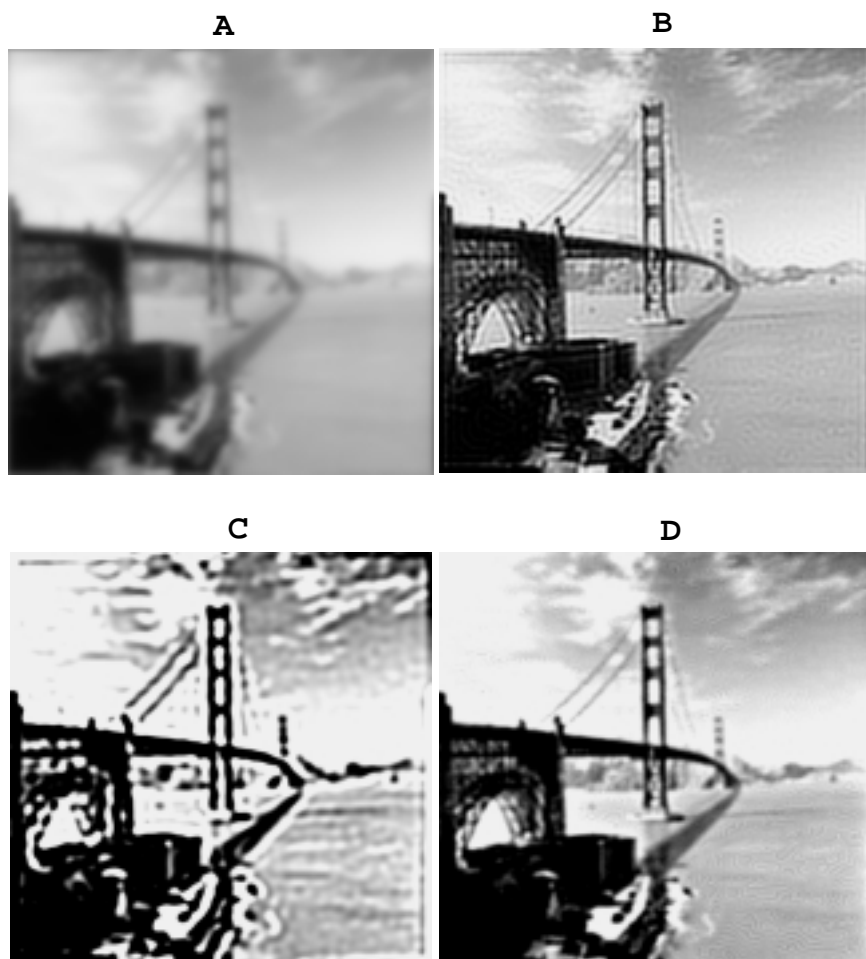


FIG. 15. APEX method in blind deblurring of blurred Golden Gate Bridge image. (A) Blurred image with  $\alpha = 0.009$ ,  $\beta = 0.75$ , stored in 8-bit precision. (B) SECB deblurring of image (A) using  $s = 0.001$ ,  $K = 0.5$ , and approximately correct parameters  $\alpha = 0.01$ ,  $\beta = 0.769$  obtained by least squares fit in Figure 14(B) with apex =  $-5.75$ . (C) SECB deblurring of image (A) using  $s = 0.001$ ,  $K = 0.5$ , and false psf with  $\alpha = 0.332$ ,  $\beta = 0.378$  obtained by least squares fit in Figure 14(C) with apex =  $-3.5$ . Wrong psf produces severe ringing. (D) SECB deblurring with false psf as in (C), but with "marching backward in time" process in (4.8) terminated at  $t = 0.5$ . (Image (C) corresponds to  $t = 0$ .) Visual quality in image (D) is better than in image (B).

itations due to noise are removed. Such an idealized experiment is useful in assessing the rationality of expecting that suitable psfs may be identified by varying the constant  $A$  in (8.2). For this purpose, eight sharp images from Figures 2 and 3 were blurred with class **G** psfs, and the blurred images were stored in 32-bit precision. These blurred images are shown in Columns A in Figure 16. With 24-bit imagery currently available, such an experiment is not devoid of practical interest. The APEX method with the marching backward in time option was used to deblur this diverse set of images. As shown in columns B, high quality detailed reconstructions were achieved. Significantly, in almost all cases, the detected psf that restored the image was *not* equivalent to the one used to blur the image.

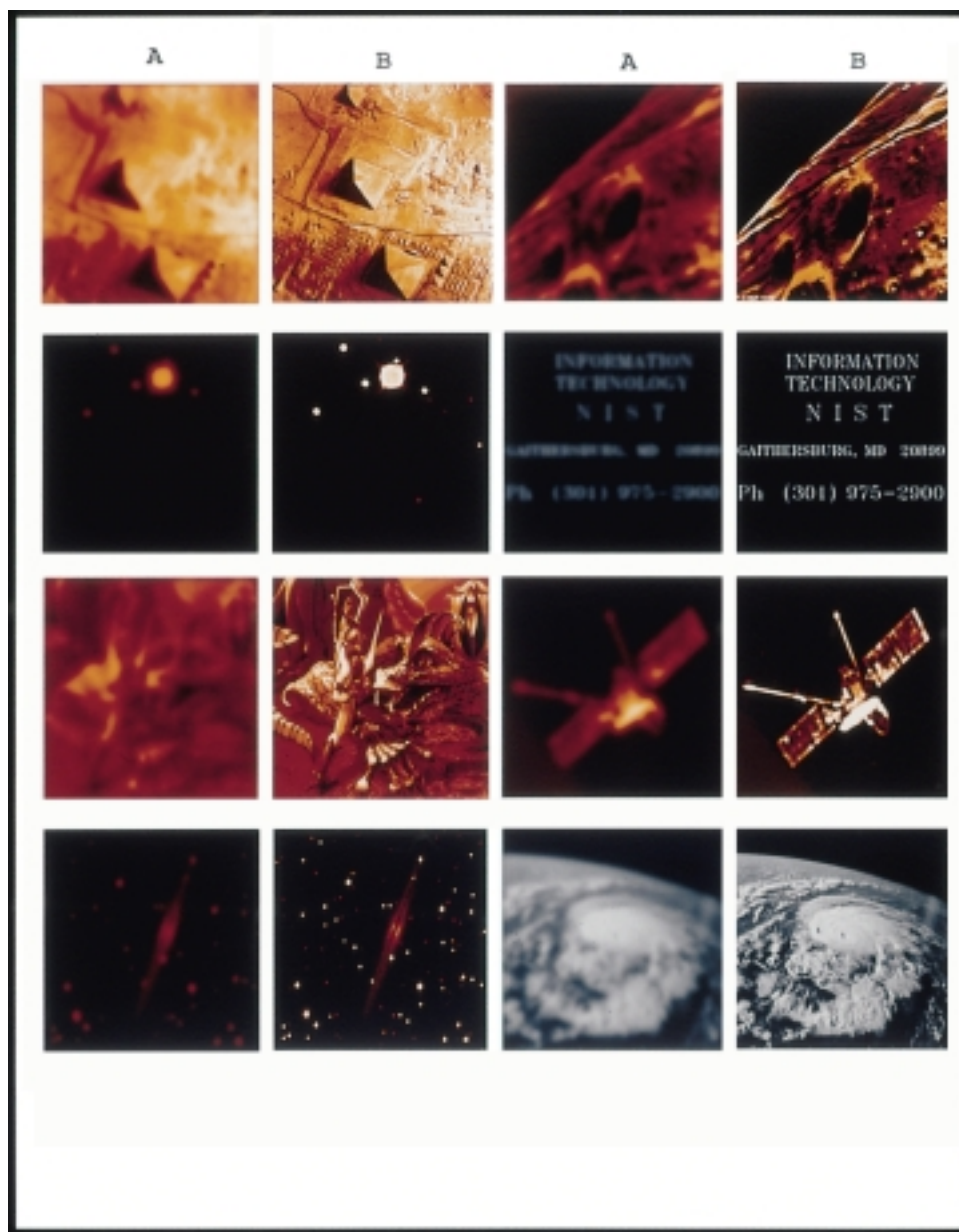


FIG. 16. Idealized APEX experiment with no noise. Blurred images in columns A were stored in 32-bit precision. Deblurred images in columns B were obtained with APEX detected psfs that differed substantially from the psfs used to create columns A. First row: Pyramids of Giza and Mars moon Phobos. Second row: Uranus and its moons and alphanumeric image. Third row: Dragon image and Mariner spacecraft. Fourth row: Edge on galaxy and hurricane image.

**9. Conclusion.** By limiting attention to the class  $\mathbf{G}$  of point spread functions, a new approach to blind deconvolution has been developed whereby the psf detection problem is detached from the image reconstruction problem. Two methods of detection were proposed, each based on 1-D Fourier analysis of blurred image data. The first method, the BEAK method, requires prior knowledge of the gross behavior in the unknown sharp image along a single line through the origin in the Fourier plane. A large class of images was exhibited, the class  $\mathbf{W}$ , for which such prior knowledge reduces to two positive numbers. This method often returns psfs that are approximately equivalent to the true system psf. The second method, the APEX method, may be applied without this prior knowledge but solves a somewhat different problem, namely, that of finding a psf that leads to a useful reconstruction. Several such psfs exist in general. The APEX method requires interactive adjustment of parameters in a manner analogous to the manual tuning of an FM station or the manual focusing of binoculars. Thus, prior knowledge of a different kind underlies the APEX method. It takes the form of user recognition or rejection of the restored image, and it is applied at the end of the reconstruction phase rather than at the beginning of the detection phase. This approach is rendered feasible through use of the fast, direct SECB deblurring method.

Except for Gaussians and Lorentzians, Lévy densities are not known in closed form as functions of the spatial variables  $x, y$ . Their relatively simple functional forms in Fourier space naturally suggest methods that operate in the Fourier domain. In particular, this enables the detection procedures to search through the entire family of Lévy densities in an efficient way.

These ideas may be extended to classes of psfs other than the class  $\mathbf{G}$ . For example, imaging problems where the psf is a weighted sum of Gaussians of different widths, or a sum of Gaussians and Lorentzians, may be considered. More generally, problems where  $\hat{h}(\xi, \eta)$  is circularly symmetric and can be expressed in functional form with a few unknown parameters may be susceptible to the above approach through 1-D Fourier analysis. The governing equation corresponding to (8.1) becomes

$$(9.1) \quad \log |\hat{g}^*(\xi, 0)| \approx \log |\hat{h}(\xi, 0)| + \log |\hat{f}_e^*(\xi, 0)|, \quad 0 \leq |\xi| \leq \omega.$$

If  $u(\xi)$  is an approximation to the gross behavior of  $\log |\hat{f}_e^*(\xi, 0)|$ , nonlinear least squares fitting of  $\log |\hat{g}^*(\xi, 0)|$  on  $0 \leq |\xi| \leq \omega$  with  $v(\xi) = \log |\hat{h}(\xi, 0)| + u(\xi)$  may be used to find values for the unknown parameters in  $\hat{h}(\xi, 0)$ . Such extensions will be considered in future reports.

Nevertheless, important problems exist that remain inaccessible by this technique. Such problems include speckle imaging in astronomy [22], where short-exposure images are degraded by atmospheric turbulence. While long-exposure turbulent distortions have been successfully modeled by Lévy densities with  $\beta = 5/6$  [18], or by Gaussians, little is known about such instantaneous turbulent point spread functions. Problems of this nature must await development of methods that can solve the blind deconvolution problem in full generality.

#### REFERENCES

- [1] G. R. AYERS AND J. C. DAINITY, *Iterative blind deconvolution method and its applications*, Optics Letters, 13 (1988), pp. 547–549.
- [2] P. BILER AND W. A. WOYCZYŃSKI, *Global and exploding solutions for nonlocal quadratic evolution problems*, SIAM J. Appl. Math., 59 (1998), pp. 845–869.

- [3] A. S. CARASSO, *Image restoration and diffusion processes*, SPIE Proceedings, 2035 (1993), pp. 255–266.
- [4] A. S. CARASSO, *Overcoming Hölder continuity in ill-posed continuation problems*, SIAM J. Numer. Anal., 31 (1994), pp. 1535–1557.
- [5] A. S. CARASSO, *Error bounds in nonsmooth image deblurring*, SIAM J. Math. Anal., 28 (1997), pp. 656–668.
- [6] A. S. CARASSO, *Linear and nonlinear image deblurring: A documented study*, SIAM J. Numer. Anal., 36 (1999), pp. 1659–1689.
- [7] A. S. CARASSO, *Logarithmic convexity and the “slow evolution” constraint in ill-posed initial value problems*, SIAM J. Math. Anal., 30 (1999), pp. 479–496.
- [8] A. S. CARASSO, *Direct blind deconvolution II. Substitute images and the BEAK method*, SIAM J. Appl. Math., submitted.
- [9] T. F. CHAN AND C. WONG, *Total variation blind deconvolution*, IEEE Trans. Image Process., 7 (1998), pp. 370–375.
- [10] J. C. DAINTY AND J. R. FIENUP, *Phase retrieval and image reconstruction for astronomy*, in Image Recovery: Theory and Application, H. Stark, ed., Academic Press, New York, 1987, pp. 195–230.
- [11] B. L. K. DAVEY, R. G. LANE, AND R. H. T. BATES, *Blind deconvolution of noisy complex-valued image*, Optics Communications, 69 (1989), pp. 353–356.
- [12] J. D. DRUMMOND, *The adaptive optics Lorentzian point spread function*, SPIE Proceedings, 3353 (1998), pp. 1030–1037.
- [13] W. FELLER, *An Introduction to Probability Theory and Its Applications*, Vol. II, 2nd ed., Wiley, New York, 1971.
- [14] D. A. FISH, A. M. BRINICOMBE, E. R. PIKE, AND J. G. WALKER, *Blind deconvolution by means of the Richardson-Lucy algorithm*, J. Opt. Soc. Amer. A, 12 (1995), pp. 58–65.
- [15] M. H. HAYES, *The unique reconstruction of multidimensional sequences from Fourier transform magnitude or phase*, in Image Recovery: Theory and Application, H. Stark, ed., Academic Press, New York, 1987, pp. 231–275.
- [16] A. HECKERT AND J. J. FILLIBEN, *DATAPLOT Reference Manual*, <http://www.itl.nist.gov/div898/software/dataplot/document.htm>.
- [17] R. HILFER, ED., *Applications of Fractional Calculus in Physics*, World Scientific, River Edge, NJ, 2000.
- [18] R. E. HUFNAGEL AND N. R. STANLEY, *Modulation transfer function associated with image transmission through turbulent media*, J. Opt. Soc. Amer., 54 (1964), pp. 52–61.
- [19] C. B. JOHNSON, *Classification of electron-optical device modulation transfer function*, Advances in Electronics and Electron Physics, 33B (1972), pp. 579–584.
- [20] R. L. LAGENDIJK AND J. BIEMOND, *Iterative Identification and Restoration of Images*, Kluwer Academic Publishers, Norwell, MA, 1991.
- [21] R. G. LANE AND R. H. T. BATES, *Relevance for blind deconvolution of recovering Fourier magnitude from phase*, Optics Communication, 63 (1987), pp. 11–14.
- [22] R. G. LANE, *Blind deconvolution of speckle images*, J. Opt. Soc. Amer. A, 9 (1992), pp. 1508–1514.
- [23] E. LUKACS, *Characteristic Functions*, Hafner, New York, 1960.
- [24] B. C. MCCALLUM, *Blind deconvolution by simulated annealing*, Optics Communications, 75 (1990), pp. 101–105.
- [25] M. NIETO-VESPERINAS, *A study of the performance of nonlinear least squares optimization methods in the problem of phase retrieval*, Optica Acta, 33 (1986), pp. 713–722.
- [26] Y. YANG, N. P. GALATSANOS, AND H. STARK, *Projection-based blind deconvolution*, J. Opt. Soc. Amer. A, 11 (1994), pp. 2401–2409.
- [27] Y. YOU AND M. KAVEH, *A regularization approach to joint blur identification and image restoration*, IEEE Trans. Image Process., 5 (1996), pp. 416–428.